A Theoretical and Experimental Comparison of Aluminum as an Energetic Additive in Solid Rocket Motors with Thrust Stand Design

A Thesis

Presented for the

Master of Science

Degree

The University of Tennessee, Knoxville

Derek Damon Farrow

August 2011

Copyright © 2011 by Derek Farrow

All rights reserved

Dedication

This thesis is dedicated to all my family and friends who through years of painstaking effort have made me into who I am today, and the good lord above for giving me the aptitude to do what I do.

Acknowledgements

I would like to thank my entire defense committee for all their input and guidance in creating this thesis. I would like to express my gratitude to Joel, Gary, and all the guys at the shop for helping me gather materials and investing their time into my work. I would also like to make a special thank you to Mr. Keith Walker for his invaluable advice and interest in this research. A final thank you goes out to Gary Flandro, and NASA for granting me the funding to be able to pursue this work.

Abstract

The use of aluminum as an energetic additive in solid rocket propellants has been around since the 1950's. Since then, much research has been done both on the aluminum material itself and on chemical techniques to properly prepare aluminum particles for injection into a solid propellant. Although initial interests in additives were centered on space limited applications, performance increases opened the door for higher performance systems without the need to remake current systems. This thesis aims to compare the performance for aluminized solid rocket motors and non-aluminized motors, as well as focuses on design considerations for a thrust stand that can be created easily at low cost for initial testing. A theoretical model is created for predicting propellant performance and the results are compared with experimental data taken from the thrust stand as well as existing data. What is seen at the end of testing is the non-aluminized grains follow the same trends as previously conducted tests and firings. The aluminized grains follow their expected trend but at a lower performance level due to grain degradation. However, the aluminized grains still show a specific impulse increase of 6%-23% over the non-aluminized grains.

Table of Contents

Chapter 1. Introduction 1

1.1. History 1

1.2. Advantages and Disadvantages 2

1.3. Procedure & Objective 4

Chapter 2. Theoretical Design 5

2.1. Overview 5

2.2. Assumptions 5

2.3. Propellant Mass Flow Rate 6

2.4. Regression Rate 6

2.5. Combustion Index Stability 8

2.6. Erosive Burning 8

2.7. Nozzle Mass Flow Rate 8

2.8. Combustion Chamber Propellant Mass Flow Rate 10

2.9. Conservation of Mass 10

2.10 Combustion Volume 12

2.11 Thrust 12

2.12 Grain Temperature Sensitivity 14

2.13 Specific Impulse 14

2.14 Validation 14

Chapter 3. Experimental Design and Testing 17

3.1. Safety 17

3.2. Propellant Specifics 17

3.3 Rig Design 18

3.3.1 Vertical Firing Thrust Stands vs. Horizontal Firing Thrust Stands 18

3.3.2 Final Thrust Stand Design 21

3.4 Motor Casing 21

3.5 Flange Design 22
3.6 Nozzle Design 26
3.7 Ignition Method 27
3.8 Seals 30
3.9 Experimental Method 30
3.9.1 Preface 30
3.9.2 Motor Firing #1 34
3.9.3 Motor Firing #2 39
3.9.4 Motor Firing #3 41
3.9.5 Motor Firing #4 43
3.9.6 Motor Firing #5 45
3.9.7 Motor Firing #6 47
3.9.8 Motor Firing #7 49
3.9.9 Motor Firing #8 51
3.10 Summary 53
Chapter 4. Discussion and Conclusion 54
4.1 Preface 54
4.2 Experimental Comparisons 54
4.2.1 Non-Aluminized Theoretical vs. Experimental Comparisons 54
4.2.2 Aluminized Theoretical vs. Experimental Comparisons 56
4.2.3 Aluminized Theoretical vs. Non-Aluminized Experimental Comparisons 57
4.2.4 I_{sp} Comparisons 57
4.3 Thrust Stand Evaluation 59
4.4 Future Work 59
List of References 61
Appendices 63
Vita 85

List of Tables

Table 2.1: Comparison of Theoretical Model with Previously Observed Data 16

Table 3.1: Motor Casing Materials 21

Table 3.2: Materials for Solid Rocket Motor Nozzle Insulator and Supporting Structure 27

Table 3.3: Experimental Data Collected 53

Table 4.1: Non-Aluminized Theoretical vs. Experimental Comparisons 56

Table 4.2: Aluminized Theoretical vs. Experimental Comparisons 56

Table 4.3: I_{sp} Comparisons 59

Table A.1: Existing Motor Performance 64

Table A.2: Available Propellant Characteristics 67

Table A.3: Variation of Calculated Performance Parameters for an Aluminized Ammonium Perchlorate Propellant as a Function of Chamber Pressure for Expansion to Sea Level 68

Table A.4: MATLAB Validation Simulation Input for Existing Motors 69

Table A.5: MATLAB Firing Simulation Input Data 70

List of Figures

Figure 1.1: Aluminum oxidization agglomerates 3

Figure 1.2: Agglomerate slag and erosion 3

Figure 2.1: Relation of burning rate to pressure and initial temperature for common propellants 7

Figure 2.2: Combustion argument for solid propellant combustion 9

Figure 2.3: Typical pressure-time curve with and without erosive burning 9

Figure 2.4: Combustion control volume for a ballistic analysis using lumped parameters 11

Figure 2.5: Combustion volume visual aid for a single end burning grain 13

Figure 2.6: Variation of chamber pressure with time for three different initial propellant grain temperatures 15

Figure 3.1: Horizontal firing thrust stand 19

Figure 3.2: Suspended flexure system 19

Figure 3.3: Custom designed vertical firing thrust stand 20

Figure 3.4: Motor casings top view 23

Figure 3.5: Motor casings side view 23

Figure 3.6: Motor casing graphite insert 24

Figure 3.7: Bottom flange 24

Figure 3.8: Top flange 25

Figure 3.9: Graphite nozzle top view 28

Figure 3.10: Graphite nozzle side view 28

Figure 3.11: Nozzle seated in top flange 29

Figure 3.12: Electric match 29

Figure 3.13: Pre-burn motor casing assembly and seals 31

Figure 3.14: Baggie igniter 33

Figure 3.15: Baggie igniter test - $5g\ BKNO_3$ performance values as a function of time [s] 33

Figure 3.16: Motor firing #1 theoretical performance values as a function of time [s] 35

Figure 3.17: Motor firing #1 experimental performance values as a function of time [s] 35

Figure 3.18: Sheared nozzle 36
Figure 3.19: Pinned back plate 36
Figure 3.20: Flow expansions 37
Figure 3.21: Steel plate burn out 37
Figure 3.22: Motor firing #2 theoretical performance values as a function of time [s] 40
Figure 3.23: Motor firing #2 experimental performance values as a function of time [s] 40
Figure 3.24: Motor firing #3 theoretical performance values as a function of time [s] 42
Figure 3.25: Motor firing #3 experimental performance values as a function of time [s] 42
Figure 3.26: Motor firing #4 theoretical performance values as a function of time [s] 44
Figure 3.27: Motor firing #4 experimental performance values as a function of time [s] 44
Figure 3.28: Motor firing #5 theoretical performance values as a function of time [s] 46
Figure 3.29: Motor firing #5 experimental performance values as a function of time [s] 46
Figure 3.30: Motor firing #6 theoretical performance values as a function of time [s] 48
Figure 3.31: Motor firing #6 experimental performance values as a function of time [s] 48
Figure 3.32: Motor firing #7 theoretical performance values as a function of time [s] 50
Figure 3.33: Motor firing #7 experimental performance values as a function of time [s] 50
Figure 3.34: Motor firing #8 theoretical performance values as a function of time [s] 52
Figure 3.35: Motor firing #8 experimental performance values as a function of time [s] 52
Figure 4.1: Non-aluminized theoretical and experimental comparisons of chamber pressure as a function of time [s] 55
Figure 4.2: Non-aluminized theoretical and experimental comparisons of thrust as a function of time [s] 55
Figure 4.3: Aluminized prediction and non-aluminized experimental comparisons of chamber pressure as a function of time [s] 58
Figure 4.4: Aluminized prediction and non-aluminized experimental comparisons of thrust as a function of time [s] 58

Nomenclature

Indices

i

j

Symbols[$\boldsymbol{Units}$]

$a\left[\frac{in^{2n+1}}{lbf^{n}\cdot s}\right]$	Initial propellant temperature coefficient
$A[\,]$	Empirical Coefficient
$A^{*}[in^{2}]$	Throat area
$A_b[in^{2}]$	Propellant grain burning area
$A_e[in^{2}]$	Nozzle exit cross sectional area
$F[lbf]$	Total thrust
$\gamma[\,]$	Specific heat ratio
$g_o\left[\frac{ft}{s^{2}}\right]$	Standard acceleration of gravity at sea level on earth
$I_{sp}[s]$	Specific impulse
$L[in]$	Length of the grain
$\dot{m}_c\left[\frac{lbm}{s}\right]$	Combustion chamber mass flow rate
$\dot{m}_n\left[\frac{lbm}{s}\right]$	Nozzle mass flow rate
$\dot{m}_p\left[\frac{lbm}{s}\right]$	Propellant mass flow rate
$n[\,]$	Burning rate exponent
$\pi[\,]$	$Pi = 3.14159$
$p_0\left[\frac{lbf}{in^{2}}\right]$	Combustion chamber pressure
$P_0\left[\frac{lbf}{in^{2}}\right]$	Combustion chamber pressure
$\rho_b\left[\frac{lbm}{in^{3}}\right]$	Solid propellant density prior to motor start
$\rho_0\left[\frac{lbf}{in^{2}}\right]$	Combustion chamber gas density

$P_A \left[\frac{lbf}{in^2}\right]$	Atmospheric pressure
$P_e \left[\frac{lbf}{in^2}\right]$	Nozzle exit pressure
$r \left[\frac{in}{s}\right]$	Burning surface regression rate
$r_i[in]$	Total distance regressed up to the current instant in time
$R \left[\frac{in^2}{s^2 \circ R}\right]$	Specific gas constant
$R_I[in]$	Grain inner radius
$R_O[in]$	Grain outer radius
$T_1[\,]$	Empirical Coefficient
$T_0[^\circ R]$	Combustion chamber temperature
$T_p[f(x)$ of emperical coefficients$]$	Initial propellant temperature
$v_e \left[\frac{ft}{s}\right]$	Nozzle exit velocity
$V_0[in^3]$	Combustion chamber volume

Chapter 1

Introduction

1.1 History

The use of aluminum as a performance enhancer in solid rocket propellants was first used in the early 1950's. While working under contract for the US Navy, two engineers from the Atlantic Research Corporation named Keith Rumbel and Charles Henderson succeeded where other scientists had failed. Contemporary theory of the day had shown that slight increases in specific impulse could be accomplished by adding small amounts of aluminum, less than 5% by weight, to solid propellants. Due to the minor performance increase predicted by this theory, however, little research had been spent on aluminized propellants. Undiscouraged, Rumbel and Henderson continued with their own series of experiments to add large amounts of aluminum, 21% by weight, to a castable composite propellant. Their results indicated a dramatic increase in the exit velocity of the solid rocket combustion gases that compared well with the performance of liquid fuels like kerosene burned in liquid oxygen (Walker, 2005).

At the time of this discovery, the Navy was preparing to place the first generation of strategic missiles aboard submarines. The Navy had planned to use solid rocket propulsion systems aboard ships to avoid the complexity and safety problems inherent with liquid fueled rockets. Unfortunately, preliminary design studies had indicated that these intercontinental ballistic missiles would have to be very large to achieve the range required to reach targets within the Soviet Union. Larger missiles meant larger submarines would be needed to carry them, and the costs of these systems would increase significantly (Walker, 2005).

The research in aluminized propellants proved to be a vital breakthrough that made the Navy's missile submarines practical. Thanks to this new technology, the Navy was able to develop smaller missiles carrying the same sized warheads over the same range. These smaller missiles could be carried aboard smaller vessels and were far safer to operate and maintain at sea than a liquid fuel system. Rumbel and Henderson's research resulted in the deployment of the Polaris A1, the first ever submarine-launched ballistic missile. Today, aluminum is one of the most researched additives for solid-fuel formulations (Walker, 2005).

1.2 Advantages and Disadvantages:

The use of aluminum as an energetic additive has several inherent advantages:

1) More Stable Burning. As solid aluminum is combusted, it oxidizes and forms large (up to 500μm diameter) agglomerates, as shown in figure 1.1. These agglomerates are pulled off the burning surface by the surrounding combustion gases and pulled down through the chamber and out the nozzle while still burning. These agglomerates in the chamber can be beneficial since the molten chunks tend to dampen out combustion instabilities that may occur. This can reduce the pressure spikes experienced in the motor and create a steadier, even burning propellant (Risha, Evans, Boyer, & Kuo, 2007).

2) Higher Efficiency. The increase in solid rocket performance that aluminum provides is due to the material's combustion properties. Aluminum burns at over 3,000 K. At these temperatures, the burning aluminum releases a large amount of energy that increases the combustion chamber pressure and forces the exhaust gases to escape through the nozzle at a much higher exit velocity. The higher exit velocity, in turn, raises the specific impulse of the motor (Risha, Evans, Boyer, & Kuo, 2007).

3) Higher Density. This leads to a higher mass flow rate into the combustion chamber and, in turn, a higher chamber pressure. Again, this leads to a higher specific impulse.

These advantages, however, do not come without some disadvantages:

1) Slag. After the solid aluminum is combusted, it will form aluminum oxide (Al_2O_3 or alumina) at the burning surface. While most of the smaller alumina particles follow the path of the combustion gases through the nozzle, the momentum of the larger particles often causes them to collide with the walls of the motor casing and nozzle. The molten aluminum can also collect in a pool in a submerged nozzle configuration and slosh around within the submergence as can be seen in figure 1.2. Due to the high temperature, these molten pools often react with the composite casing causing premature decomposition of the motor walls (Risha, Evans, Boyer, & Kuo, 2007).

2) Nozzle Clogging. Viscous forces can also pull the pooled molten aluminum into the nozzle throat causing a partial clog of the region. This clog reduces the throat area resulting in a temporary pressure spike within the chamber (Risha, Evans, Boyer, & Kuo, 2007).

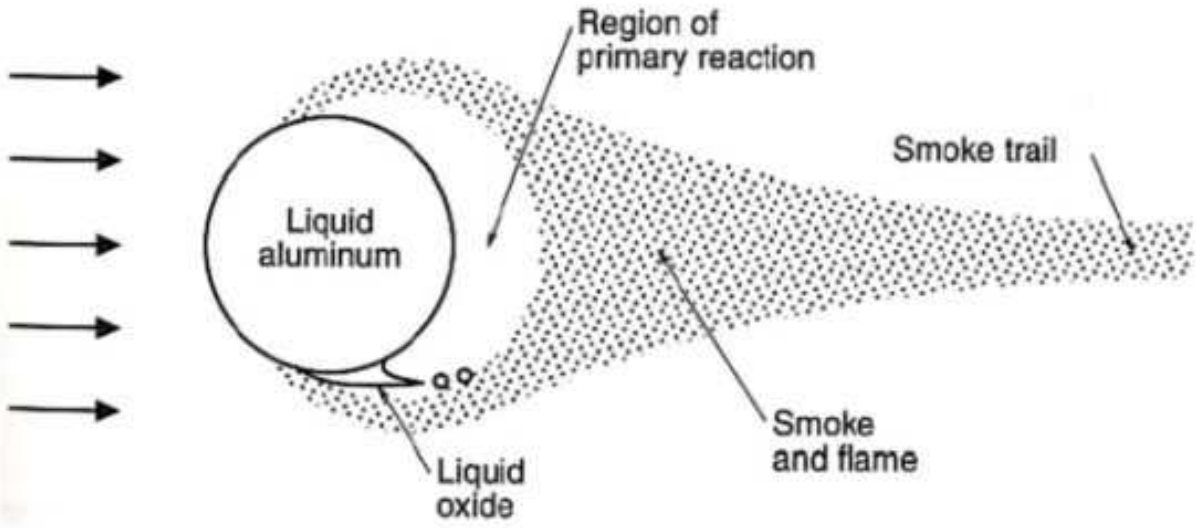

Figure 1.1: Aluminum oxidization agglomerates.

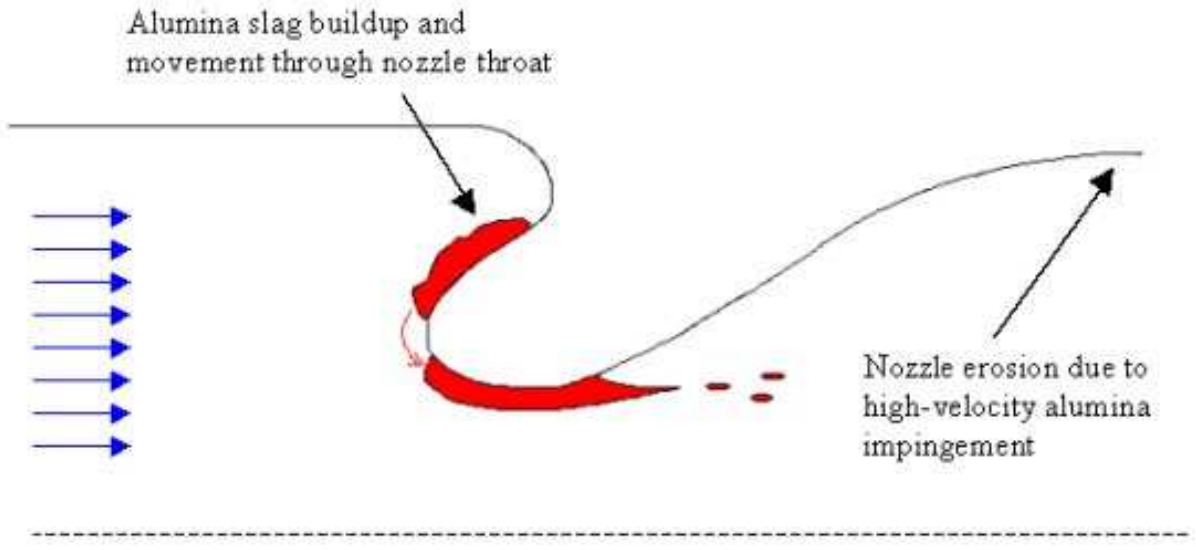

Figure 1.2: Agglomerate slag and erosion.

3) Two-Phase Flow Losses. When large agglomerate droplets form, they are traveling at relatively slow speeds compared to the exhaust gases within the combustion chamber. It takes energy to accelerate these relatively large particles to the speed of the gas flow. The energy needed to change the momentum of the aluminum agglomerates is extracted from the gases as they flow downstream. Moreover, the aluminum particles are not only being accelerated axially, but radially as well, which can rob the exhaust of considerable energy depending on the aluminum content of the propellant. In fact, two-phase flow losses can account for as much as a 5% reduction in rocket performance (Walker, 2005).

Despite the problems associated with aluminized propellant combustion, the benefits of increased specific impulse outweigh the costs.

1.3 Procedure & Objective:

The objective of this thesis was to show the performance differences between aluminized and non-aluminized propellant. First, an analytical model was developed using a time-dependant lumped parameter method. This allowed experimental and financial decisions to be made on a thrust stand design. After a design was chosen, an experimental test matrix was created for the available propellant grains. Once the motors were fired the chamber pressure and thrust was measured, the resulting performance data was analyzed and compared to pre-existing and theoretical data.

Chapter 2

Theoretical Design

2.1 Overview

Since part of the overall objective of this thesis is to build a thrust stand to measure the performance of small solid rocket motors, some financial constraints have to be adhered to. In order to accomplish this, a theoretical framework is needed. With a basic knowledge of compressible flow, a simulation of internal ballistics is created. This allows for better initial sizing of the thrust stand rather than wasting money on guesswork.

The basis of this framework is a mass balance resulting from a time-dependant lumped parameter method. By equating the mass of the propellant being injected into the combustion chamber with the mass stored in the chamber and the mass being ejected from the nozzle, an iterative process is developed using MATLAB for describing important performance parameters. It is these parameters that will provide a starting point for thrust stand sizing. A sample listing of MATLAB code used is included in Appendix 6.

2.2 Assumptions

In developing this framework, there are certain assumptions that are made for the sake of simplicity.

- Each individual propellant grain is of uniform composition and consistency.
- There is a constant combustion temperature.
- The combustion process behaves isentropically.
- The combustion process is 100% efficient, meaning there is no residual propellant being ejected out of the nozzle or left in the combustion chamber as slag.
- The combustion gases behave as an ideal gas.
- Across the combustion chamber there is a constant specific heat ratio.
- The nozzles are successfully able to choke the flow.
- Nozzle flow can be approximated as Quasi-one-dimensional.

2.3 Propellant Mass Flow Rate

The combustion chamber of a solid propellant rocket is essentially a high pressure tank containing the entire solid mass of propellant. The rate of generation of gaseous propellant is equal to the rate of consumption of solid material. Hence it is given by:

$$\dot{m}_p = A_b r \rho_b \tag{2.1}$$

where $\dot{m}_p \left[\frac{lbm}{s}\right]$ is the propellant mass flow rate, $A_b[in^2]$ is the burning area of the propellant grain, $r \left[\frac{in}{s}\right]$ is the regression rate of the burning surface, and $\rho_b \left[\frac{lbm}{in^3}\right]$ is the solid propellant density prior to motor start.

2.4 Regression Rate

The regression rate, or the rate at which the propellant burns, is an empirically determined function of the propellant composition and certain conditions within the combustion chamber. These conditions include propellant initial temperature, combustion pressure, and the velocity of the gaseous combustion products over the surface of the solid. Figure 2.1 illustrates the regression rates of several propellants as a function of pressure and initial temperature in the absence of appreciable gas velocity. This can be approximated by St. Robert's Law:

$$r = a{p_0}^n \tag{2.2}$$

where $r \left[\frac{in}{s}\right]$ is the regression rate of the burning surface, $a \left[\frac{in^{2n+1}}{lbf^{n} \cdot s}\right]$ is the initial propellant temperature coefficient, $p_0 \left[\frac{lbf}{in^2}\right]$ is the combustion chamber pressure, and n is the regression rate exponent (Hill & Peterson, 1965).

The regression rate exponent n, associated with the slope of the curves in figure 2.1, is almost independent of propellant temperature. The coefficient a is a function of initial propellant temperature but not a function of pressure. Usually, a is expressed as:

$$a = \frac{A}{T_1 - T_p} \tag{2.3}$$

where T_1 and A are empirical constants, and $T_p[f(x)$ of emperical coefficients] is the initial propellant temperature (Hill & Peterson, 1965). Since the regression rate expression contains empirical coefficients,

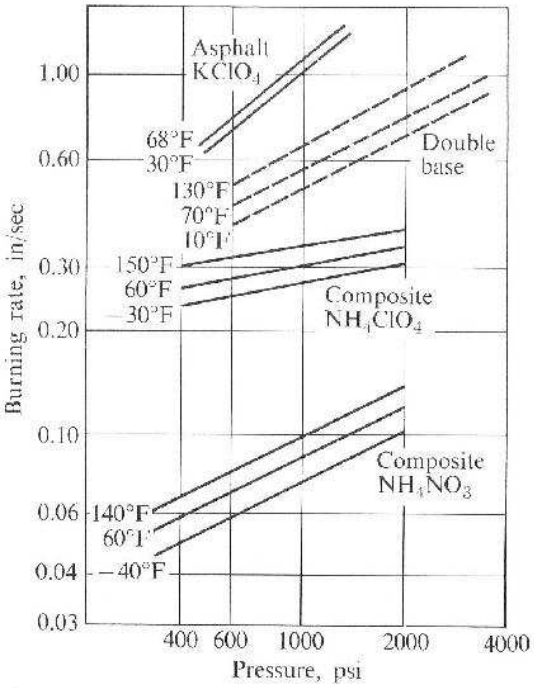

Figure 2.1: Relation of burning rate to pressure and initial temperature for common propellants (Hill & Peterson, Mechanics and Thermodynamics of Propulsion, 1965).

care will have to be taken when choosing values. This will be explained more thoroughly in a later section.

2.5 Combustion Index Stability

Classically, the regression rate exponent n must be less than unity for stable combustion, as may be demonstrated by the following simple argument. Neglecting the relatively small gas storage terms, nozzle flow rate and gas generation rate must be equal. Equation 2.2 shows that the regression rate and hence, gas generation rate is directly proportional to ${p_0}^n$. Figure 2.2 indicates typical curves of nozzle flow rate and gas generation rate versus pressure. Two gas generation rate curves, one for $n < 1$ and one for $n > 1$, are shown, both having the same operating point with the given nozzle. Consider a small decrease from the operating-point pressure. It can be seen that for $n < 1$ the resultant gas generation rate will then exceed the nozzle flow rate, and thus the chamber pressure will return toward the original value. For $n > 1$, any small decrease in chamber pressure means that nozzle flow rate will exceed gas generation rate and the pressure will drop even further. Thus for $n > 1$, small disturbances are amplified and the combustion cannot be stable. Hence for stable combustion, n must be less than unity (Hill & Peterson, Mechanics and Thermodynamics of Propulsion, 1965).

2.6 Erosive Burning

Another assumption that will be made is the lack of erosive burning effects. When propellant gases flow parallel to the burning surface of a solid propellant, the regression rate of the propellant at a given pressure is increased. Due to erosive burning, the additional mass flow rate increases the combustion chamber pressure. This behavior can be seen in figure 2.3.

2.7 Nozzle Mass Flow Rate

In order to develop an expression for the nozzle mass flow rate, the concept of "choked flow" needs to be understood. When a fluid, at a given pressure and temperature flows through a restriction, in this case a nozzle throat, into a lower pressure area, the fluid velocity increases. At initially subsonic upstream conditions, the law of conservation of mass requires the fluid velocity to increase as it flows through the smaller cross-sectional area of the throat. Choked flow is a limiting condition which naturally occurs when the mass flow rate will not increase with a further decrease in the downstream pressure environment while upstream pressure is fixed. Using this choked flow definition, Anderson (Anderson, 2004) defines the mass flow rate through the nozzle as:

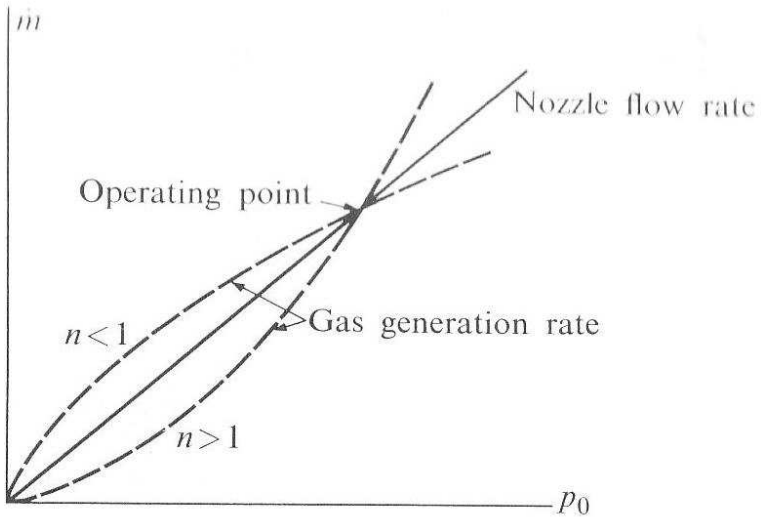

Figure 2.2: Combustion argument for solid propellant combustion (Hill & Peterson, Mechanics and Thermodynamics of Propulsion, 1965).

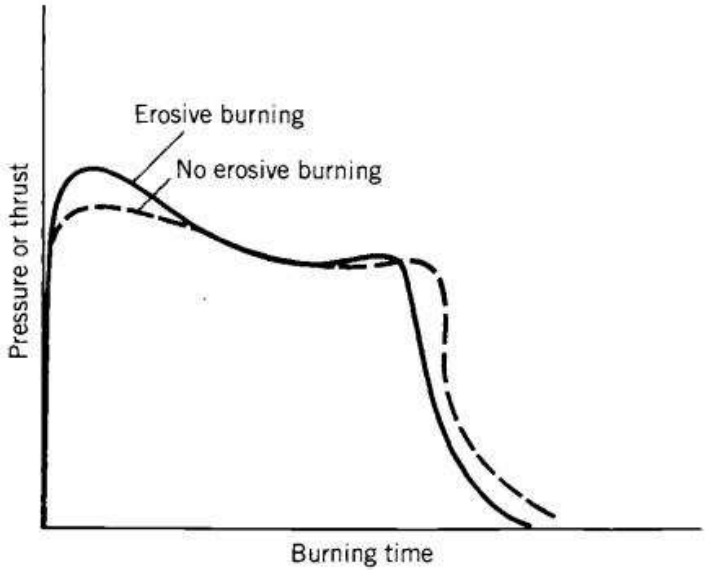

Figure 2.3: Typical pressure-time curve with and without erosive burning (Biblarz & Sutton, 2001).

$$\dot{m}_n = \frac{P_0 A^*}{\sqrt{T_0}} \sqrt{\frac{\gamma}{R}\left(\frac{2}{\gamma+1}\right)^{\frac{\gamma+1}{\gamma-1}}} \tag{2.4}$$

where $\dot{m}_n \left[\frac{lbm}{s}\right]$ is the nozzle mass flow rate**,** $P_0 \left[\frac{lbf}{in^2}\right]$ is the combustion chamber pressure, $A^*[in^2]$ is the throat area, $T_0[°R]$ is the combustion chamber temperature, γ is the unitless specific heat ratio, and $R \left[\frac{in^2}{s^2 °R}\right]$ is the specific gas constant.

2.8 Combustion Chamber Propellant Mass Flow Rate

The combustion chamber propellant mass is given by:

$$\dot{m}_c = \frac{d}{dt}(\rho_0 V_0) \tag{2.5}$$

where $\dot{m}_c \left[\frac{lbm}{s}\right]$ is combustion chamber mass flow rate, $\rho_0 \left[\frac{lbf}{in^2}\right]$ is the combustion chamber gas density, and $V_0[in^3]$ is the combustion chamber volume (Biblarz & Sutton, 2001).

2.9 Conservation of Mass

By applying the conservation of mass across the control volume shown in figure 2.4, the propellant mass burned per unit time has to equal the sum of the change in gas mass per unit time in the combustion chamber and the mass flowing out through the nozzle. From equation 2.1, equation 2.4, and equation 2.5, it can be seen that:

$$A_b r \rho_b = \frac{d}{dt}(\rho_0 V_0) + \frac{P_0 A^*}{\sqrt{T_0}} \sqrt{\frac{\gamma}{R}\left(\frac{2}{\gamma+1}\right)^{\frac{\gamma+1}{\gamma-1}}} \tag{2.6}$$

Equation 2.6 is the mass balance of the system. One thing to notice about equation 2.6 is the fact that the chamber pressure is an average. The entire chamber pressure at any given time is represented by a single value. Classically, this is known as a "lumped parameter method". Naturally, this method is not exact; however, it gives remarkably good results without the need for in-depth combustion and pyrolysis analysis. It is here that an iterative process will be employed to determine expected performance parameters.

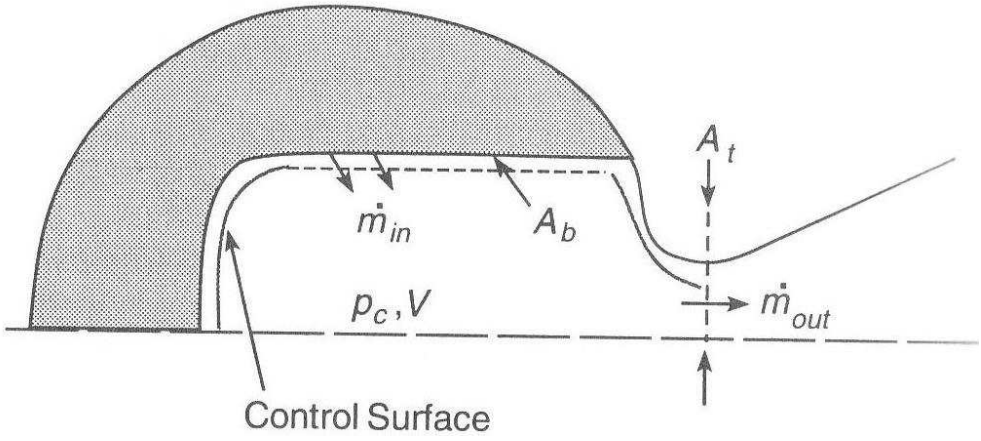

Figure 2.4: Combustion control volume for a ballistic analysis using lumped parameters (Humble, Henry, & Larson, 1995).

2.10 Combustion Volume

The motors used in these experiments are a cylindrical propellant grain with a thin tubular fiberglass outer casing around them. Because of this, a motor casing will have to be designed along with the thrust stand for firing purposes. Because of the shape:

$$V_0(i) = \pi R_I^2(i)L(i) + \pi R_O^2 \sum_{j=0}^{i-1} r_i \tag{2.7}$$

where $V_0(i)[in^3]$ is the combustion chamber volume at this instant, $R_I(i)[in]$ is the grain inner radius at this instant, $L(i)[in]$ is the length of the grain at this instant, $R_O[in]$ is the grain outer radius, $r_i[in]$ is the total distance regressed up to the current instant, and j is a counter used for indexing. A visual aid is shown in figure 2.5.

By using the regression rate of the previous instances in the summation $\sum_{j=0}^{i-1} r_i$, the previous instances and the current instant can be linked together. This is how the iterative process arises. This same formulation will be used in proceeding parameters that vary directly based on the regression rate, although they will not explicitly be shown.

Due to design decisions and specific grain geometry, which will be discussed more thoroughly in the experimental section, this experiment will only be concerned with radially burning grains. Because of this, equation 2.7 simplifies to the useable form of the combustion chamber volume:

$$V_0(i) = \pi R_I^2(i)L \tag{2.8}$$

where L is now a constant.

2.11 Thrust

Because of fixed nozzle geometry and changes in ambient pressure due to changes in altitude, there can be an imbalance of the atmospheric pressure and the local pressure of the hot gas jet at the exit plane of the nozzle. Thus, for a steadily operating rocket propulsion system moving through a homogeneous atmosphere, the total thrust is:

$$F = \dot{m}_n v_e + (P_e - P_A)A_e \tag{2.9}$$

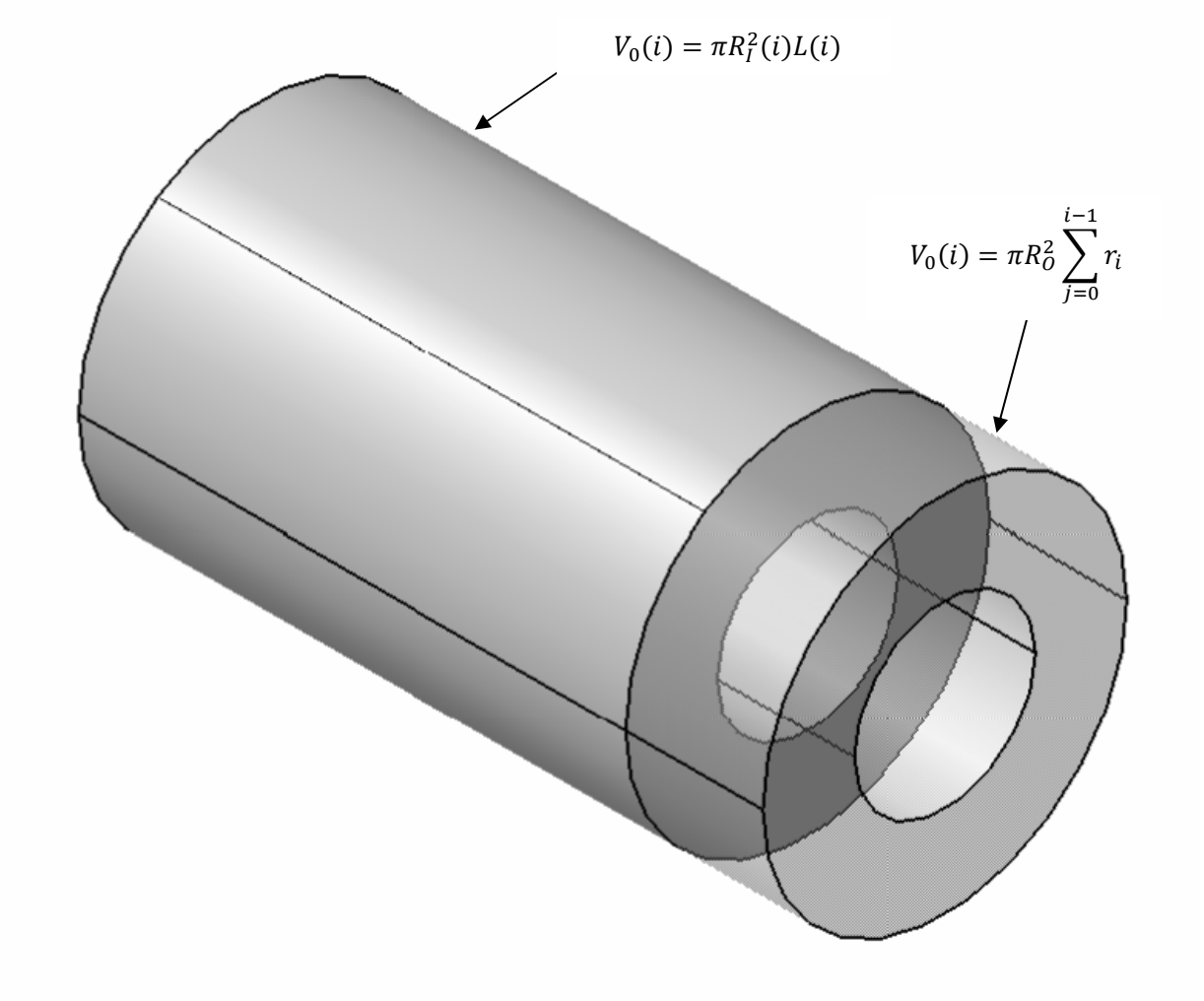

Figure 2.5: Combustion volume visual aid for a single end burning grain.

where $F\ [lbf]$ is the total thrust, $\dot{m}_n\left[\frac{lbm}{s}\right]$ is the nozzle mass flow rate, $v_e\left[\frac{ft}{s}\right]$ is the nozzle exit velocity, $P_e\left[\frac{lbf}{in^2}\right]$ is the nozzle exit pressure, $P_A\left[\frac{lbf}{in^2}\right]$ is the atmospheric pressure, and $A_e[in^2]$ is the nozzle exit cross sectional area (Anderson, 2004).

For the experiments this report is concerned with, there is no change in atmospheric pressure and P_A is taken at sea level.

2.12 Grain Temperature Sensitivity

The variation of regression rate r with temperature, indicated previously in figure 2.1 and accounted for by an equation of the form of equation 2.2, can seriously alter the performance of a given rocket under different firing-temperature conditions. For example, figure 2.6 indicates the time variation of chamber pressure for three different initial temperatures. The thrust histories would be similar since thrust is proportional to p_0. However, since at constant T_0 the mass flow rate will also be proportional to p_0, the thrust duration will be inversely proportional to p_0. Hence the total impulse, $\int Tdt$, will be practically constant regardless of propellant temperature. However, excessive variation of regression rate can have serious consequences. If it is too high, structural failure can occur. If it is too low, insufficient thrust may prevent satisfactory performance (Hill & Peterson, 1965).

2.13 Specific Impulse

Specific impulse is a unitless performance parameter used for direct comparisons between different propulsion systems without regard to their detailed inner workings. Specific impulse is defined as the total impulse per unit weight of propellant flow:

$$I_{sp} = \frac{F}{\dot{m}_n g_o} \tag{2.10}$$

where $I_{sp}[s]$ is the specific impulse, $F[lbf]$ is the total thrust, $\dot{m}_n\left[\frac{lbm}{s}\right]$ is the nozzle mass flow rate, and $g_o\left[\frac{ft}{s^2}\right]$ is the standard acceleration of gravity at sea level on earth (Biblarz & Sutton, 2001).

2.14 Validation

In order to test this model, the results are compared to existing motors that data is readily obtainable for. The motors that will be compared are the Star-48, First Stage Minuteman Missile Motor (Thiokol M55), and the Star-27. Finally, substituting in the propellant characteristics, dimensions, and nozzle specifics for these motors given in Appendix 1 into the theoretical model and comparing the performance, the accuracy

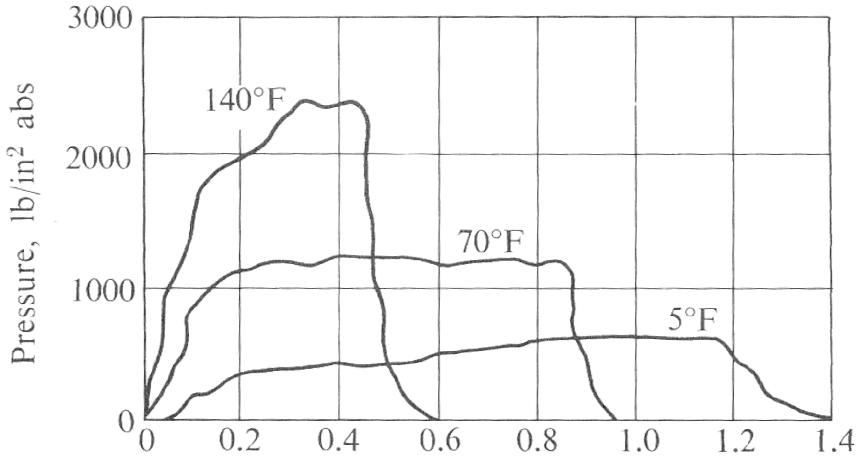

Figure 2.6: Variation of chamber pressure with time for three different initial propellant grain temperatures (Hill & Peterson, 1965).

of the theoretical model can be examined. This is shown in table 2.1. Appendix 3 also lists more existing data used for comparison.

Table 2.1

Comparison of Theoretical Model with Previously Observed Data

	Star-48B*	**Theoretical**	**% Difference**
Chamber Pressure [psi]	579	538	7.08
Regression Rate [in/s]	.194	.189	2.58
Vacuum Thrust [lbf]	13,239	13,347	.82
Specific Impulse [s]	294.2	325.8	10.7
	Thiokol M55**	**Theoretical**	**% Difference**
Chamber Pressure [psi]	780	783.5	.45
Regression Rate [in/s]	.349	.324	7.16
Thrust [lbf]	194,600	205,500	5.60
Specific Impulse [s]	254	259	1.97
	Star-27**	**Theoretical**	**% Difference**
Chamber Pressure [psi]	502	484	3.59
Regression Rate [in/s]	.28 @ $1{,}000psi$	.198	---
Thrust [lbf]	6,010	5,665	5.7
Specific Impulse [s]	290.8	324	11.4

* - (Alliant Techsystems Inc., 2008)
** - (Biblarz & Sutton, 2001)

One thing to note about table 2.1 is the performance data for the Star-27 motor. The listed regression rate for this motor has been published using a $1{,}000psi$ chamber pressure whereas the chamber pressure, thrust, and specific impulse are using an unpublished regression rate. Overall, however, this shows that the theoretical model gives sufficiently accurate results to be used as a tool for initial designs of a thrust stand.

Chapter 3

Experimental Design and Testing

3.1 Safety

No matter how sure one is of predictive calculations, the very nature of experimental work is unstable, and sometimes, unsafe. In order to establish safety guidelines, research needs to be done on available propellant capabilities. Since the composition of the most energetic propellant (the aluminum based grains) is very close to those used in the motors listed in Appendix 1, this is an appropriate place to begin looking at safety concerns. By examining the data in this appendix, one can see two very important values.

First, the adiabatic flame temperature of these propellants are approximately 6000°F. This is easily hot enough to overcome the melting point of steel (~2500°F), aluminum (~1250°F), and titanium (~3050°F) which are three of the most popular materials used in aerospace applications. No matter what the final design of the thrust stand is, care must be taken to make sure the components of the stand are sealed together properly. Any gaps could allow the 6000°F propellant flow to be diverted from exiting through the nozzle and to act as a blowtorch cutting through part of the stand and anything around it.

The second thing to be wary of is the combustion chamber pressure. With expected pressures up to 1000 psi and a nozzle choking the flow to make sure there is a buildup of chamber pressure used to generate thrust, the thrust stand has now turned into a potential bomb. The developed analytical model is used along with preexisting experimental data and a generous factor of safety of two in order to prepare for any misfires that could lead to personal injury or property damage. In addition to these safety precautions the motors will be ignited by a pair of remote leads that will place the operators safely away from the firing zone.

3.2 Propellant Specifics

The experiments performed for this report are centered on 4 different types of propellant grains. These are ammonium perchlorate based grains with aluminum as an additive and those

without aluminum. Also, some of the propellant grains come in different sizes. This information is shown in Appendix 2.

3.3 Rig Design

3.3.1 Vertical Firing Thrust Stands vs. Horizontal Firing Thrust Stands

Now that there is an analytical model available, it is used in sizing considerations for the thrust stand. For thrust stand designs, there are two primary types. The first type is a horizontal firing thrust stand. Horizontal firing stands expel the exhaust gases in a direction parallel to the ground. The second type is a vertical firing thrust stand. Vertical stands align the motor exhaust either towards the ground or straight up into the air.

There are several advantages and disadvantages to each configuration, but in practice it boils down to two disadvantages. Horizontal firing stands, as seen in figure 3.1, suffer from a movement impediment along the axial direction from any kind of restraint used to anchor the motor casing to the rest of the stand during firings. This resistance to motion can adversely affect thrust measurements. Although most of the effort for this problem (for small motors) is focused on roller and bearing systems used to reduce horizontal friction between the motor casing and the stand during the burn, there is no way to completely remove it. The most widely accepted way to get data in a setup like this (for large motors) is by suspending the casing in the air via flexures as shown in figure 3.2. This approach is too expensive and overly complicated for current needs, so it is an unlikely candidate. The second type of stand is a vertical firing stand. Vertical firing stands, as seen in figure 3.3, do not have the friction or complication issues encountered by horizontal stands. Vertical stands are placed on top of a thrust measurement device with some variety of guide rods (or other acceptable methods) around the perimeter to keep it upright. These rods do add a bit of resistance to movement to the system, but this is very minor. The primary concern with vertical stands is a bit more subtle because the issue lies within the data collected. With a vertical configuration one measures the weight of the motor casing, the structure, and the propellant grain itself. Initially, instead of having a zero thrust measurement, one has a reading of the total weight supported by the load cell, which is rated at $1000lbf \pm .06\%$. (Omega Engineering, Inc., 2011). This is acceptable; since one can zero this out through

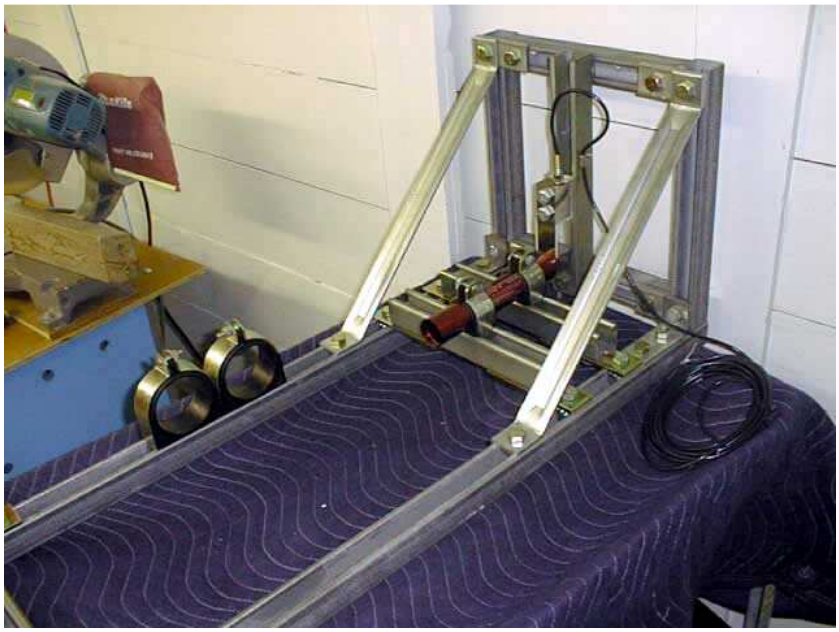

Figure 3.1: Horizontal firing thrust stand (Aerocon Systems).

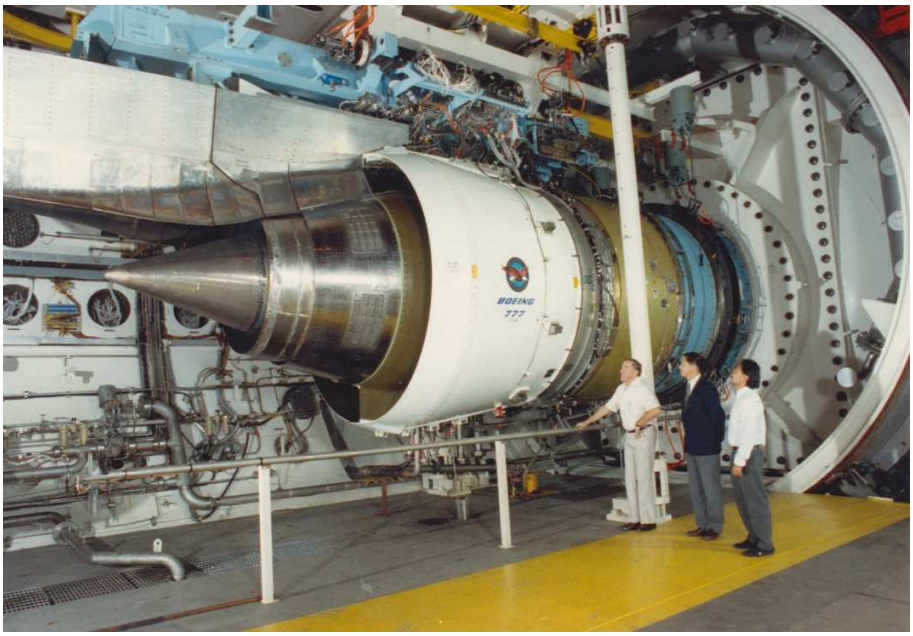

Figure 3.2: Suspended flexure system (Arnold Air Force Base).

Figure 3.3: Custom designed vertical firing thrust stand.

the Data Acquisition System (DAQ). However, during the burn the system will have a time-varying mass due to the propellant grain being burned. This will cause an error in thrust measurement, since the data being recorded will include the thrust produced by the system plus the weight of the system from the burning propellant. This can be a serious problem in larger motors or in experiments where one is trying to get very precise thrust measurements from a specific propellant grain configuration, neither of which are of any consequence to this report. Based on the arguments above, a vertical firing stand was selected.

3.3.2 Final Thrust Stand Design

The design finally selected was shown in figure 3.3 with schematics shown in Appendix 7. All subsequent discussion on design considerations will be focused on this type of thrust stand. As seen in the final design, the accepted design does not specifically employ a method to guard against shrapnel. It was decided to save on cost and weight and conduct the tests from a location where no one or anything can be hurt or damaged.

3.4 Motor Casing

The motor case acts as a pressure vessel to contain the high-pressure combustion processes occurring within the bore of the motor. Cases may be constructed from metal materials, from composite fiber material, or from a combination of a metal "liner" with a composite overwrap. Table 3.1 summarizes some of the critical properties of various candidate materials.

Table 3.1

Motor Casing Materials

Material	**Density** $\left[\frac{lbm}{in^3}\right]$	**Ultimate Tensile Strength** $[ksi]$	**Young's Modulus** $[msi]$
2219-Aluminum	.101	60	10
Titanium	.161	178	15
D6AC Steel	.283	220	29
4130 Steel	.283	125	29
Graphite	.056	140-250	10-20
Kevlar	.05	120-160	6-8
Fiberglass	.072	160	4.7

(Humble, Henry, & Larson, 1995)

Many lower-cost solid rocket motors use metal designs that are simple to build, especially if the motor is quite small or has to be reusable. Many small motors in air-launched missiles employ steel cases using either the 4130 alloy or the higher strength D6AC (or Maraging) alloy. Small and mid-size space motors have often employed titanium cases. Aluminum is an attractive choice as a case material for only the smallest motors because of its low strength (Humble, Henry, & Larson, 1995).

As highlighted in Table 3.1, the composite materials are very attractive case materials because of their high strength-to-weight ratios. Motor cases designed with these materials can be 20%-30% lighter than conventional metal cases. Some of the mass savings is lost because these materials are not as stiff as titanium or steel, so large deflections are possible. Often, stiffness concerns of this type override strength considerations, thus increasing the mass of the composite case above its minimum value solely to retain internal pressure.

Since the propellant grains in these experiments are small, the motor cases are made of aluminum. These cases can be seen in figures 3.4 and 3.5. Since there are two different outer diameters of available propellant grains, one motor case will be fabricated for each. This takes care of the outer diameter issue, but still leaves the issue of having four different length grains. Instead of fabricating four different casings, a set of graphite spacers was created to support the shorter grains in a single casing; an example of these spacers in seen in figure 3.6. Notice the hole in the center to allow a gas flow passage out towards the pressure transducer.

3.5 Flange Design

This design is built upon two steel flanges. The bottom flange rests on the load cell and also houses the pressure probe. Both of the motor casings are fitted to sit in a recess bored into both flanges as seen in figure 3.7 for the bottom flange. Figure 3.7 also shows the location of the pressure tap and hole in the center of the interior surface of the flange that connects to the pressure probe. The top flange is identical to the bottom; however, there is no pressure probe system. Instead, the top flange has a counter bored hole for sitting the nozzle into. This is shown in figure 3.8. Both flanges have eight holes drilled along the outside of the flange that allows for eight $\emptyset.875\ in$ all threaded bolts to be used for tightening the system. Finally, there are four small holes for $\emptyset.515\ in$ guide rods that keep the system sitting properly on the load cell.

Figure 3.4: Motor casings top view.

Figure 3.5: Motor casings side view.

Figure 3.6: Motor casing graphite insert.

Figure 3.7: Bottom flange.

Figure 3.8: Top flange.

3.6 Nozzle Design

Much of the design, analysis, and fabrication time for a solid rocket motor lie in developing the nozzle. The nozzle converts high thermal energy of chamber gases to directed kinetic energy and thrust. For this reason, the highest velocities, heat fluxes and pressure gradients are in this part of the motor. Studies of historical solid rocket motor failures show that roughly 50% of all failures occur from problems in the nozzle area. The high failure rate in this area is attributed to the severe environment and the fact that some nozzles can contain many parts and may have to vector to control the vehicle's direction. Analysis of nozzle behavior is also difficult because both thermal and structural loads are important to the overall state of stress in this region.

Solid rocket motor nozzles are constructed of composite materials, metals, and polymers. Current throat materials are primarily polycrystalline graphite or 3-D carbon-carbon (Humble, Henry, & Larson, 1995). Carbon- and graphite-phenolic are used in larger throats where the higher ablation rate has only a small effect on the expansion ratio and hence the I_{SP}. Also, 3-D carbon-carbon is costly for large throats while the polycrystalline graphite is difficult to produce in very large sizes without defects that may cause failure. Exit cones are principally carbon-phenolic with silica-phenolic used in lower erosion areas. There are some 2-D carbon-carbon exit cones where the cost of obtaining a lower mass is justified (Humble, Henry, & Larson, 1995).

For most common purposes a nozzle should have a high specific heat, low thermal conductivity, and a low erosion rate. Using these guidelines and table 3.2, a graphite nozzle was chosen. There are many types of graphite nozzles. Some are pure graphite while some are full of additives to finely tune the graphite to more accurately meet the specific needs of the motor. Since heavy nozzle weights, long motor burn times, and large motor sizes are not relevant to this set of experiments, a pure chunk of graphite machined into a nozzle is adequate as long as the nozzle doesn’t erode during the burns. This, however, will not be known until experimentation begins, and the nozzle will have to be inspected for ablation after every firing.

Now that a nozzle material has been chosen, fabrication and sizing can be explored. The nozzle has two requirements that must be met. First, it must fit into the top flange as defined in section 3.5 and Appendix 7. Second, the throat must be a specified diameter. Typically, much

Table 3.2

Materials for Solid Rocket Motor Nozzle Insulator and Supporting Structure

Material	**Density** $\left[\frac{kg}{m^3}\right]$	**Specific Heat** $\left[\frac{cal}{gm \cdot K}\right]$	**Thermal Conductivity** $\left[\frac{W}{m \cdot K}\right]$	**Ultimate Tensile Strength** $[MPa]$	**Erosion Rate*** $\left[\frac{mm}{s}\right]$
Pyrolytic Graphite	2200	.5	.059	103	.05
Polycrystalline Graphite	1700	.6	26	48	.1
2-D Carbon/Carbon	1400	.54	13.8	110	---
3-D Carbon/Carbon	1900	.5	31.5	186	.1
Carbon/Phenolic	1400	.36	1	72.4	.18
Graphite/Phenolic	1400	.39	1.59	52.4	.28
Silica/Phenolic	1700	.3	.55	52.4	1.3
Glass/Phenolic	1900	.22	.028	414	1.5
Paper/Phenolic	1200	.37	.4	152	1.9

* Data taken at: chamber pressure = 6.9 MPa, Throat diameter = .3 m, Combustion temperature = 3030K (Humble, Henry, & Larson, 1995)

work is done on nozzles to add a properly contoured diverging section for ideally full expansion after the throat. This is used to further increase the now sonic flow speed effectively increasing the thrust and I_{SP}. While thrust data was desired in these experiments, it was not of such importance that additional effort was included for a diverging section. As a starting point, three different throat diameter nozzles were created. The idea was, since there were some identical grains, different nozzle diameters would make good test cases to be used for comparisons. One of the nozzles can be seen in figures 3.9, 3.10, and already seated in the top flange in 3.11.

3.7 Ignition Method

There is lots of information written out in literature and on the internet on ignition techniques for igniting small motors. Companies that deal in smaller rockets like ESTES, Apogee, and Quest use simple electric matches. However, even among “simple” matches, there are many different types. The type that was used in these experiments is an ESTES match, as seen in figure 3.12. A voltage source is hooked up to the lead wires on the igniter and once the system gets power, the small amount of pyrotechnic powder on the head on the match will heat

Figure 3.9: Graphite nozzle top view.

Figure 3.10: Graphite nozzle side view.

Figure 3.11: Nozzle seated in top flange.

Figure 3.12: Electric match.

up rapidly and then burn away. This burning is the source of heat for igniting the grains that are to be analyzed. Initially, these tests were to be conducted with this pyrotechnic portion of the igniter hot glued directly to the propellant grain as seen in figure 3.13. In this situation though, it was found that it was very difficult to keep the pyrotechnic material pressed right up against the propellant grain while the glue was curing. So an alternative method was found. The solution used was to take the ESTES igniter and hot glue the pyrotechnic part of the igniter to a chunk of ESTES rocket motor. This propellant chunk was then hot glued to the propellant grain to be tested. This method worked successfully, but the data was not as expected and was later changed as explained in section 3.9.

3.8 Seals

The final components to be constructed are the seals. As was discussed earlier, it is a requirement that hot gas flow comes out of the nozzle, and nowhere else. With the current design, this leaves two places to be concerned with, in between the motor casing and each of the flanges. Figure 3.13 also shows the location of the seals. The sealing configuration used is an outer copper ring seal along with a double-layer lead tape seal on the inside. Two layers of lead tape are used to match the thickness of the copper seal. This same configuration is used on both the top and the bottom of the motor casing. It was unknown how these seals would hold up during use, so both were checked after every firing.

3.9 Experimental Method

3.9.1 Preface

As with most experimental procedures, there were complications in firings before acceptable data was obtained. Most of these problems stemmed from routine errors in the control program for the DAQ and it took three firings before these problems were remedied. After getting acceptable data, there was one final issue that needed to be addressed. Motor performance for these three tests was approximately 3% of expected values. This difference is attributed to the way the propellant grain burns and the ignition method used. Ideally when cylindrical propellant grains start burning, the entire inner circular circumference along the entire length of the grain will simultaneously ignite and will begin regressing radially outwards in a very uniform burn. By using an ignition method where burning is started at a single point, which

Figure 3.13: Pre-burn motor casing assembly and seals.

was tried in these firings, there is regression from the ignition point out radially (as expected) but also, along the length and around the circumference of the grain. Given enough time, all the propellant burns, but it's a much slower and undesirable burn. A better way to do the igniter is seen in figure 3.14. By taking a predefined amount of Boron-Potassium Nitrate ($BKNO_3$) and using the igniter to set off a baggie of $BKNO_3$, which has been placed down inside the propellant grain, the entire internal burning surface ignites and essentially acts as if the combustion chamber has been pre-pressurized. Pre-pressurization is desirable because it enables the propellant to ignite easier as well as lowers the ignition rise time. A decision had to be made on how much pre-pressurization is necessary for acceptable data. From Appendix 1, it is seen that these propellants function normally within the $500 - 700\ psi$ range. In order to push the operating pressure up closer to the expected pressure, the $BKNO_3$ was used. The amount of $BKNO_3$ to be used had to be determined experimentally, so in order to do the $BKNO_3$ testing without wasting propellant grains, an aluminum stock was fabricated that fits inside the motor casing and has a hole bored into the stock with the same internal diameter as the propellant grains. The $BKNO_3$ baggie igniter was then slid down to the bottom of the stock inside the motor casing. One thing to note for this setup, since the igniter was now located at the bottom of the system, leads were soldered onto the igniter ends to be long enough to hook up to the ignition system. With the stock in place, firings could take place to check the chamber pre-pressurization. Since these systems expected a chamber pressure of $500 - 700\ psi$, a $1000\ psi$ chamber pressure was desirable as a pre-pressurization. Two igniter tests were run with 5g of $BKNO_3$, but even with the smallest nozzle of $\emptyset.52\ in$, chamber pressures were approximately $150\ psi$ or less. At this point it was much easier (and cheaper) to fabricate a new nozzle than increasing the amount of $BKNO_3$ in the system. A new $\emptyset.3\ in$ nozzle was created and then fired with the standard 5g of $BKNO_3$. Coincidentally, this produced a chamber pressure of approximately $900\ psi$, close to what was desired, as can be seen in figure 3.15.

Figure 3.14: Baggie igniter.

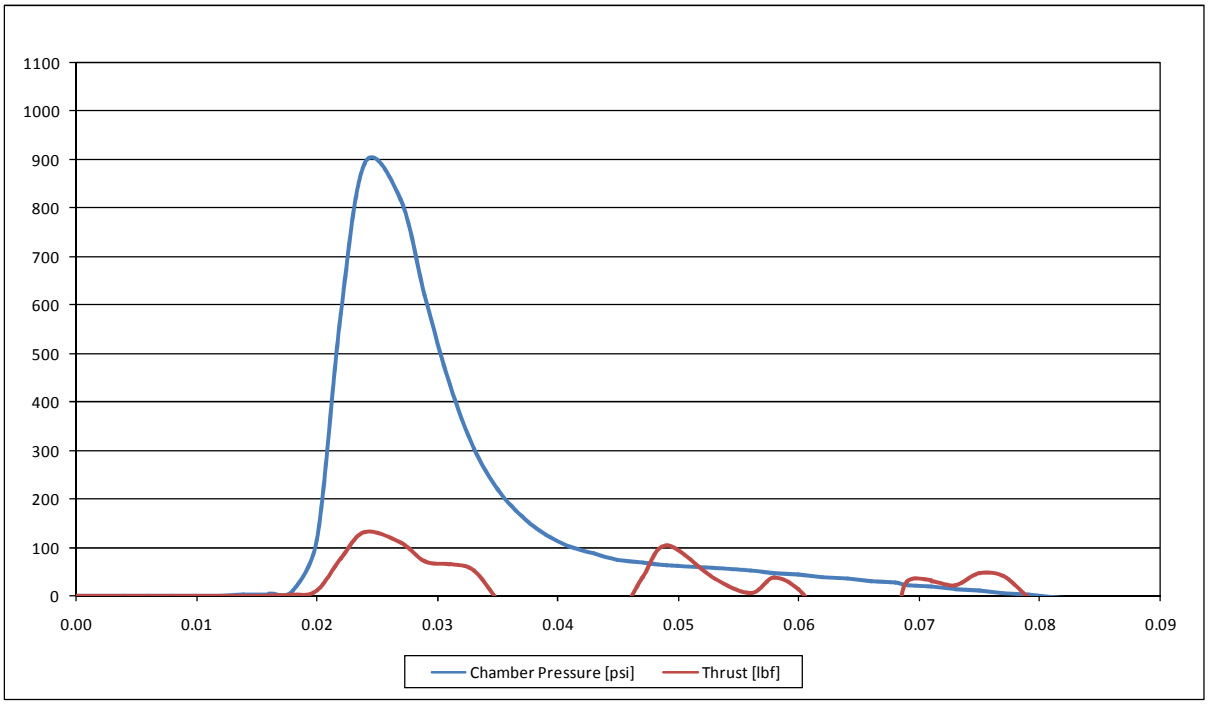

Figure 3.15: Baggie igniter test - $5g\ BKNO_3$ performance values as a function of time [s].

3.9.2 Motor Firing #1

Non-aluminized grain
ID: .5in.
OD: 2in.
L: 3.75in.
Nozzle Throat: Ø.3

Theoretical Prediction

Using the data from Appendix 1, the theoretical performance for this motor is shown in figure 3.16. Chamber pressure and thrust peaked at approximately $655\ psi$ and $56\ lbf$ respectively.

Experimental

Chamber pressure and thrust peaked at $790\ psi$ and $71\ lbf$ respectively as is seen in figure 3.17. There was a major problem with this new nozzle, however. A $1000\ psi$ burst inside the chamber sheared the nozzle in half as seen in figure 3.18. Graphite is a very strong material when in compression, but when shear forces are applied, it becomes very brittle and can break. Rather than redesign the nozzle and flange, a steel plate was machined to pin onto the top flange as shown in figure 3.19 to allow the graphite to compress. This simple solution worked fine in all subsequent testing. While this allowed the $BKNO_3$ ignition method to be used, it also presented an unexpected find. As a reminder, when these nozzles were designed they were made without a divergent section. So during a test there is hot air following a converging section into the nozzle throat where there hopefully is laminar flow. Ideally the gas flow would perfectly stick to the contour of the nozzle and the flow would be straightened and shot out of the throat parallel to the contour of the throat section. However, the throat is a section of turbulent gas flow depending on how it is reflected by other parts of the air stream and the nozzle wall. This is expected gas flow behavior when still in the throat, but what actually happened is once the throat ended, gas flow jettisoned out giving the appearance of an underexpanded flow, an example is shown in figure 3.20. The first burn after adding the steel plate, the propellant exhaust naturally carved out a diverging section in the new back plate. This can be seen in figure 3.21. From this firing onward, the experimental thrust measured was higher than the previous firings due to the new “nozzle

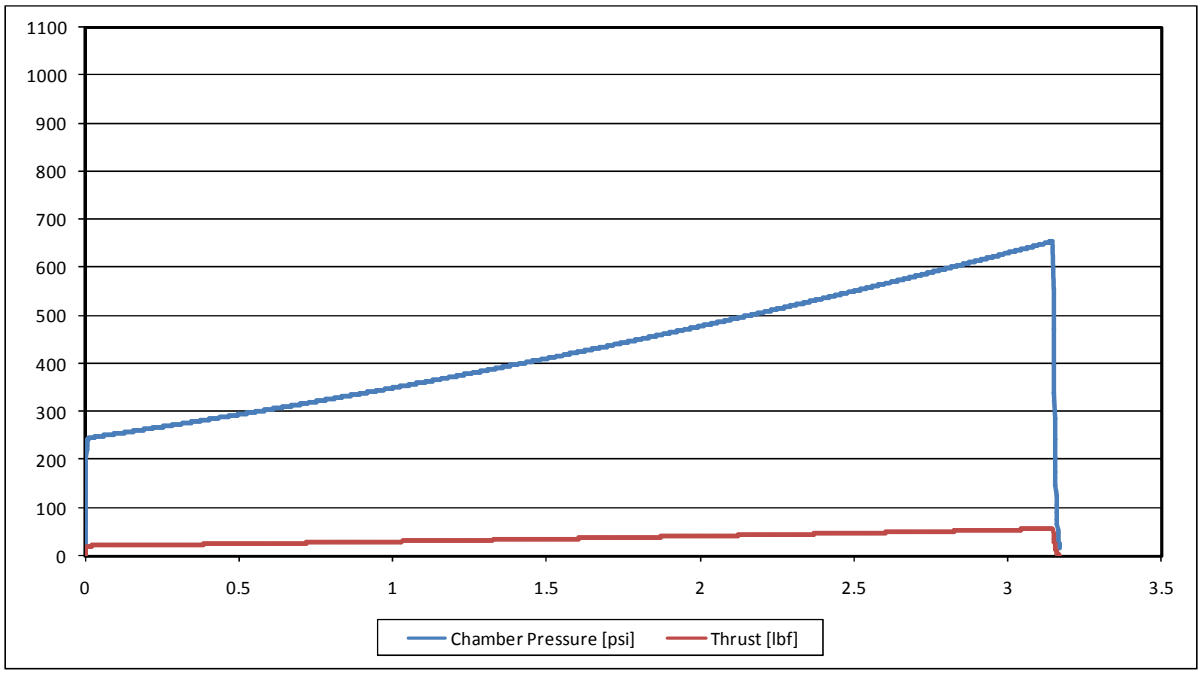

Figure 3.16: Motor firing #1 theoretical performance values as a function of time [s].

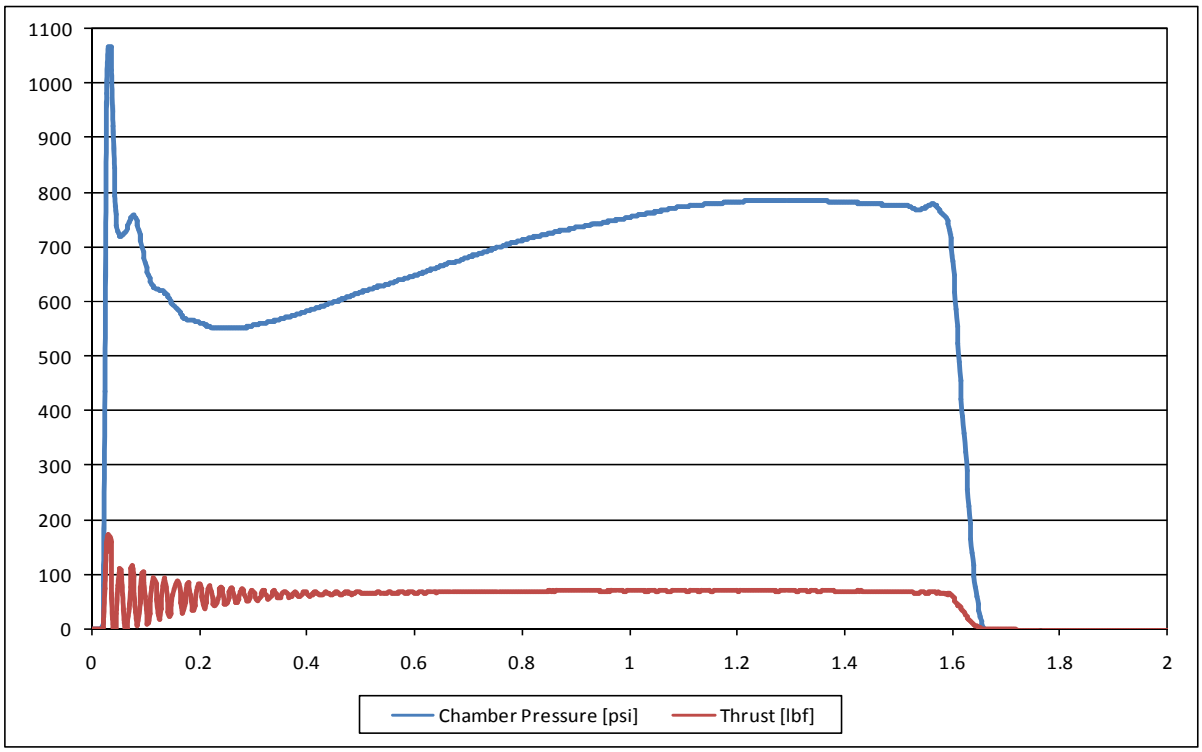

Figure 3.17: Motor firing #1 experimental performance values as a function of time [s].

Figure 3.18: Sheared nozzle.

Figure 3.19: Pinned back plate.

		During flight			During seaievel static tests		
Stage	A_2/A_t		h(km)	I_s (sec)		h(km)	I_s (sec)
Booster or first stage	6	Nozzle flows full, slight underexpansion	0	267	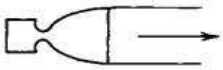 Nozzle flows full	0	267
Second stage	10	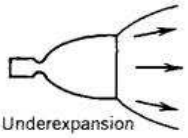 Underexpansion	24	312	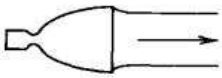 Overexpansion, slight contraction	0	254
Third stage	40	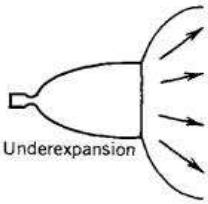 Underexpansion	100	334	Flow separation caused by overexpansion	0	245

Figure 3.20: Flow expansions.

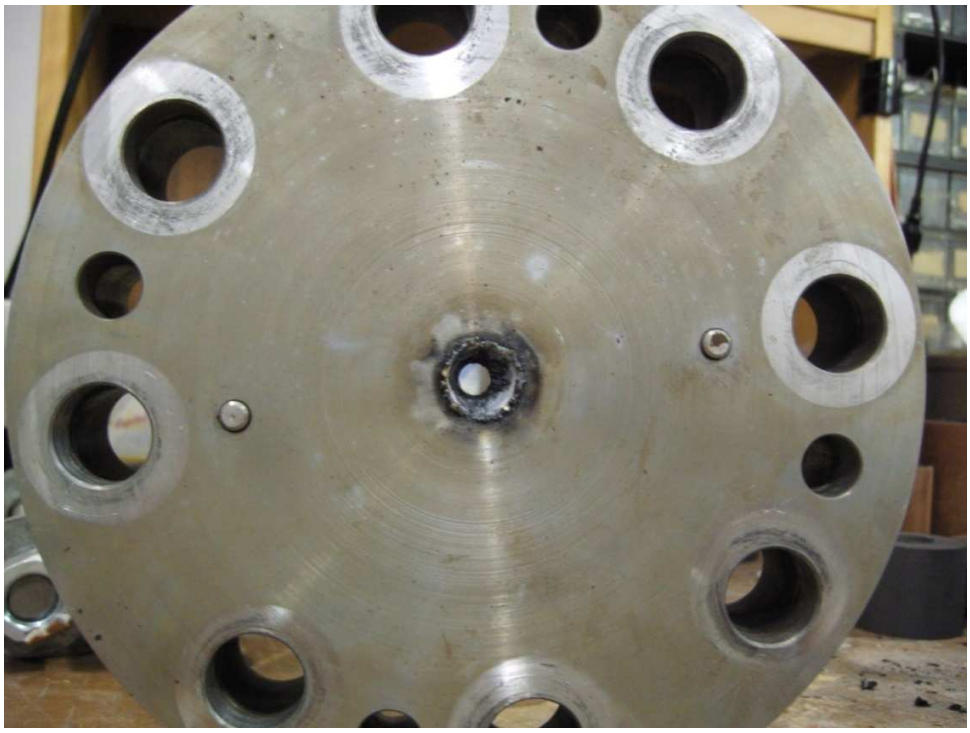

Figure 3.21: Steel plate burn out.

diverging section". By adding this increase into the theoretical model and comparing results, thrust was increased by approximately $10\ lbf$ or $14.1\ \%$. For subsequent firings, the theoretical model does not take into account the changing diverging section of the back plate due to the inability to precisely describe the contour throughout the firing.

Comments

None

3.9.3 Motor Firing #2

Aluminized grain
ID: .4375in.
OD: 2in.
L: 3.5in.
Nozzle Throat: Ø.3

Theoretical Prediction

Using the data from Appendix 1, the theoretical performance for this motor is shown in figure 3.22. Chamber pressure and thrust peaked at approximately $690\ psi$ and $50\ lbf$ respectively.

Experimental

Chamber pressure and thrust peaked at $594\ psi$ and $56\ lbf$ respectively as is seen in figure 3.23.

Comments

By comparing figures 3.22 and 3.23 it is seen that the experimental burn time is only slightly shorter than the predicted value. This firing began properly, however, after the igniter fired, there was approximately a four second interval until the propellant ignited. There are two possibilities on what happened. First, this was an aluminized grain and since these grains are rather old, there could've been an Al_2O_3 layer buildup along the grain's surface. This layer could've absorbed some of the heat from the igniter and hence delayed ignition. Secondly, the igniter simply wasn't strong enough to ignite this grain, however, after the ignition maybe a piece of molten steel fell into the grain cavity and sat there smoldering until it was able to ignite the grain. The solution could also be a combination of the previously mentioned issues. For the next aluminized firing, the grains were checked more thoroughly for Al_2O_3 buildup before firing.

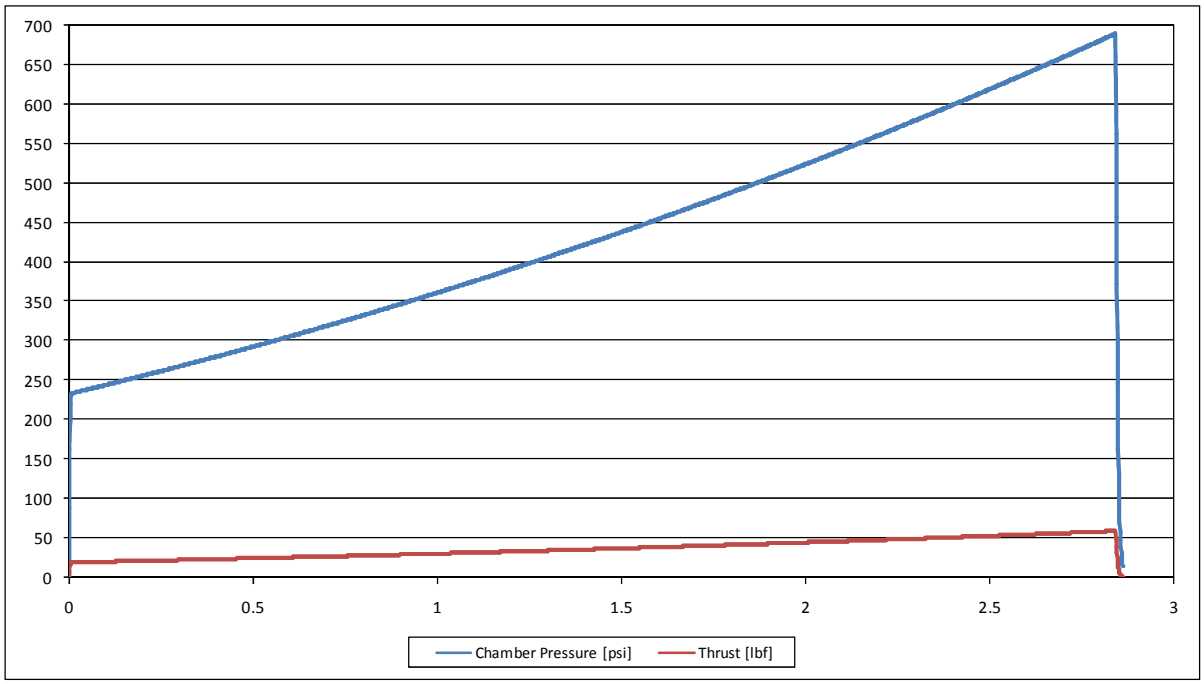

Figure 3.22: Motor firing #2 theoretical performance values as a function of time [s].

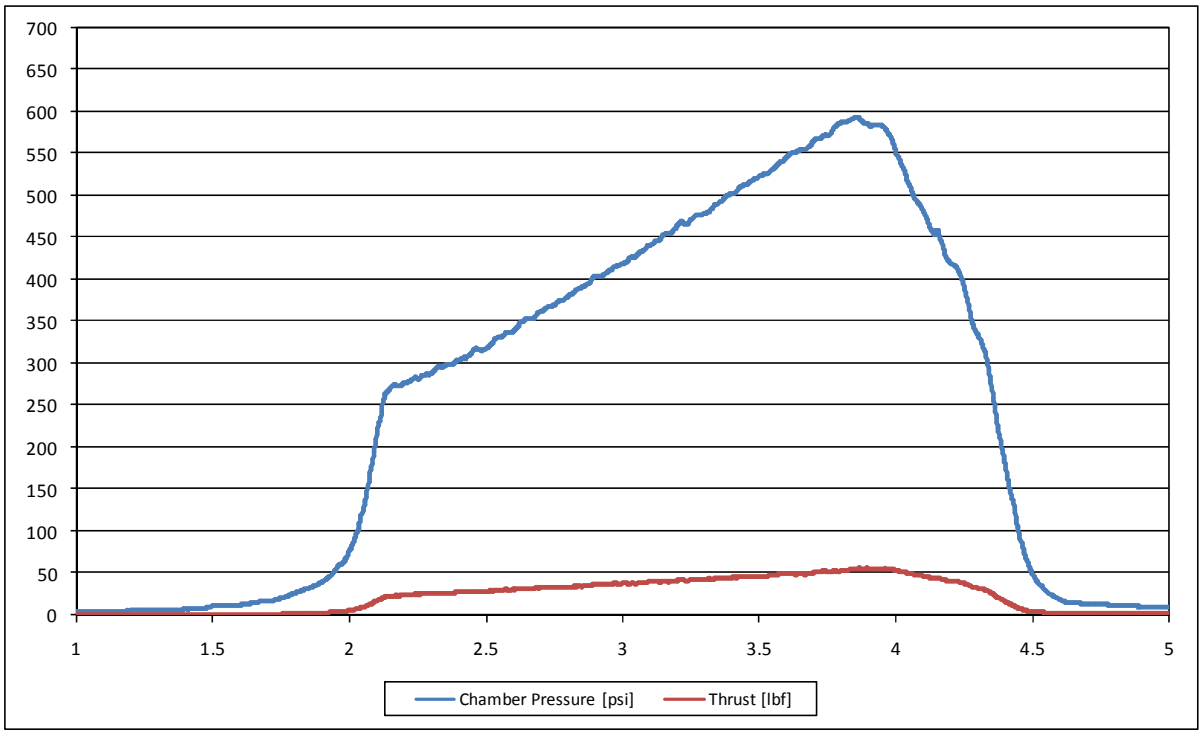

Figure 3.23: Motor firing #2 experimental performance values as a function of time [s].

3.9.4 Motor Firing #3

Non-aluminized grain
ID: .5in.
OD: 2in.
L: 3.75in.
Nozzle Throat: Ø.3

Theoretical Prediction

Using the data from Appendix 1, the theoretical performance for this motor is shown in figure 3.24. Chamber pressure and thrust peaked at approximately $655\ psi$ and $56\ lbf$ respectively.

Experimental

Chamber pressure and thrust peaked at $662\ psi$ and $74\ lbf$ respectively as is seen in figure 3.25.

Comments

None

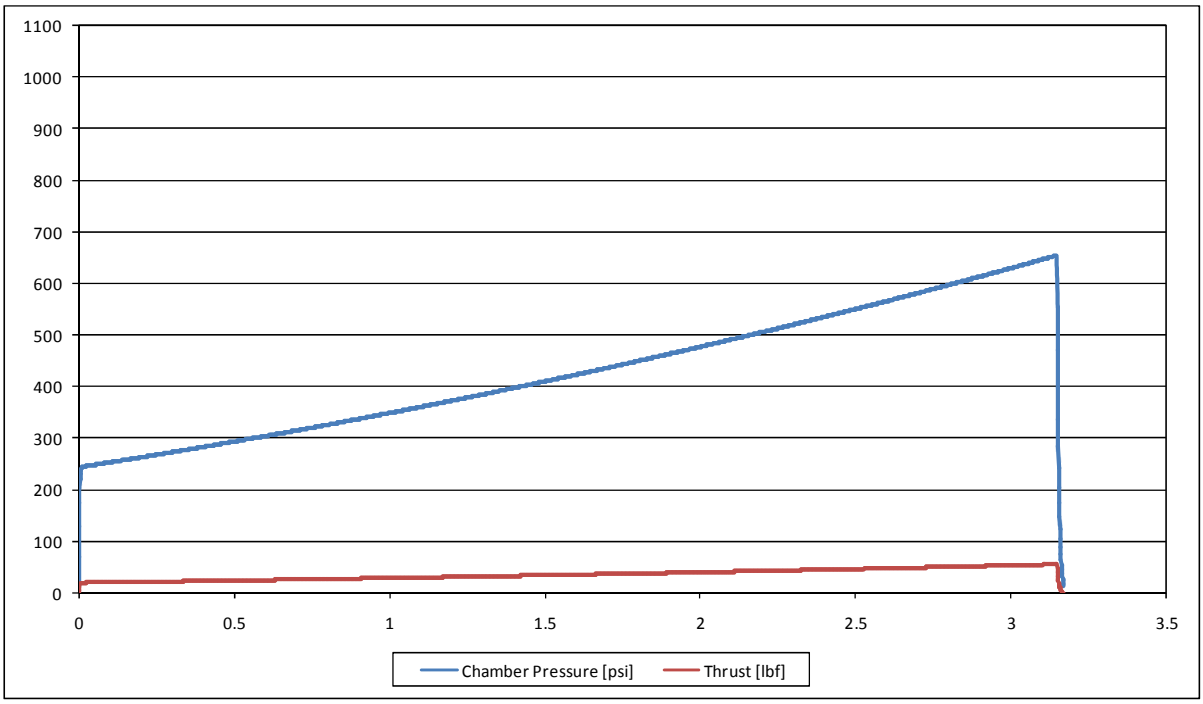

Figure 3.24: Motor firing #3 theoretical performance values as a function of time [s].

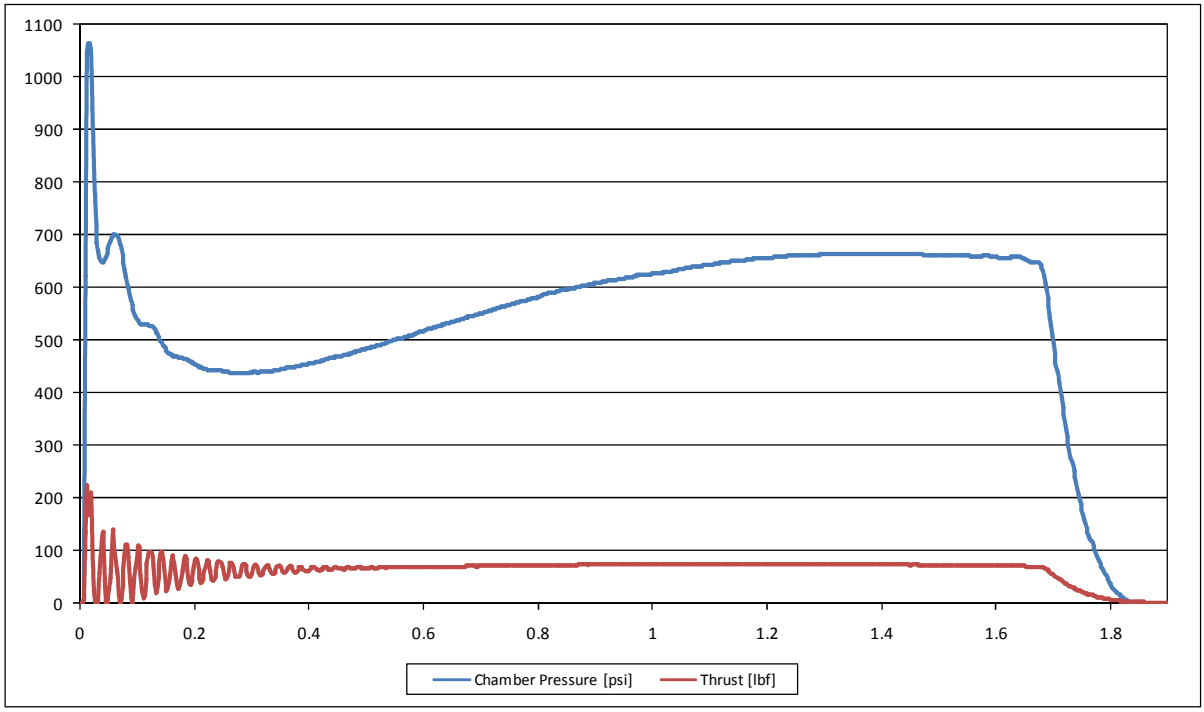

Figure 3.25: Motor firing #3 experimental performance values as a function of time [s].

3.9.5 Motor Firing #4

Non-aluminized grain
ID: .5in.
OD: 2in.
L: 3.75in.
Nozzle Throat: Ø.3

Theoretical Prediction

Using the data from Appendix 1, the theoretical performance for this motor is shown in figure 3.26. Chamber pressure and thrust peaked at approximately $655\ psi$ and $56\ lbf$ respectively.

Experimental

Chamber pressure and thrust peaked at $665\ psi$ and $72\ lbf$ respectively as is seen in figure 3.27.

Comments

None

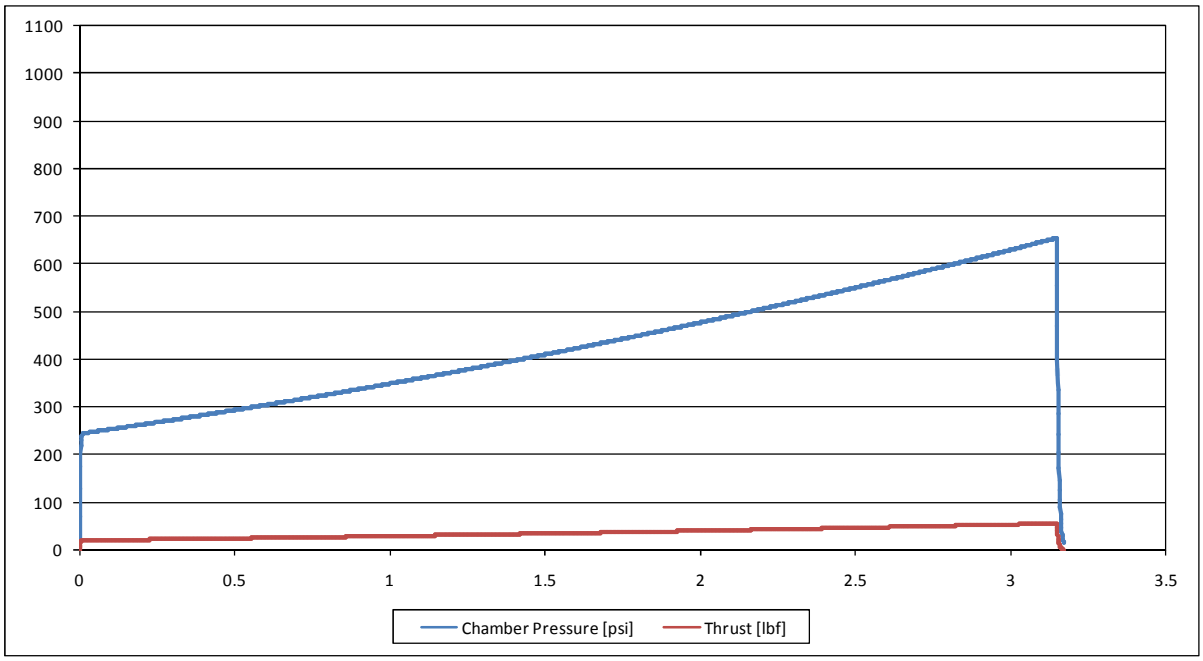

Figure 3.26: Motor firing #4 theoretical performance values as a function of time [s].

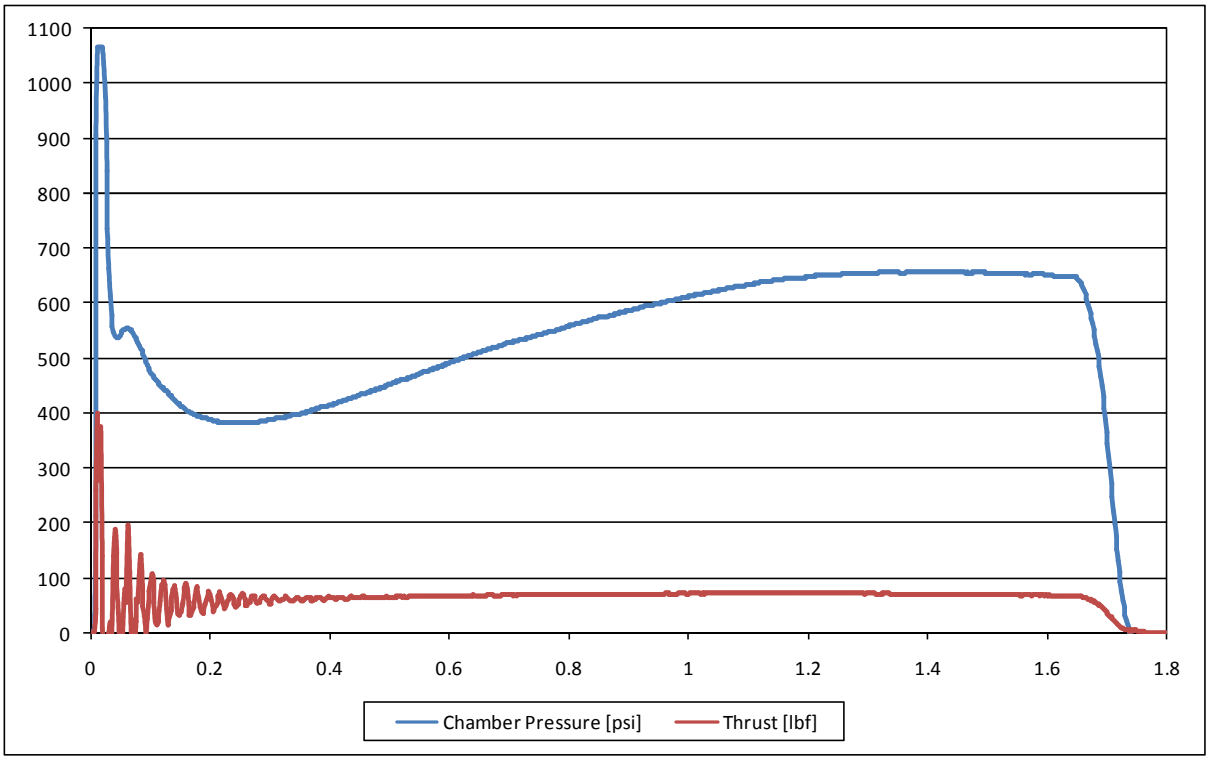

Figure 3.27: Motor firing #4 experimental performance values as a function of time [s].

3.9.6 Motor Firing #5

Non-aluminized grain
ID: .5in.
OD: 2in.
L: 3.75in.
Nozzle Throat: Ø.3

Theoretical Prediction

Using the data from Appendix 1, the theoretical performance for this motor is shown in figure 3.28. Chamber pressure and thrust peaked at approximately $655\ psi$ and $56\ lbf$ respectively.

Experimental

Chamber pressure and thrust peaked at $700\ psi$ and $63\ lbf$ respectively as is seen in figure 3.29.

Comments

None

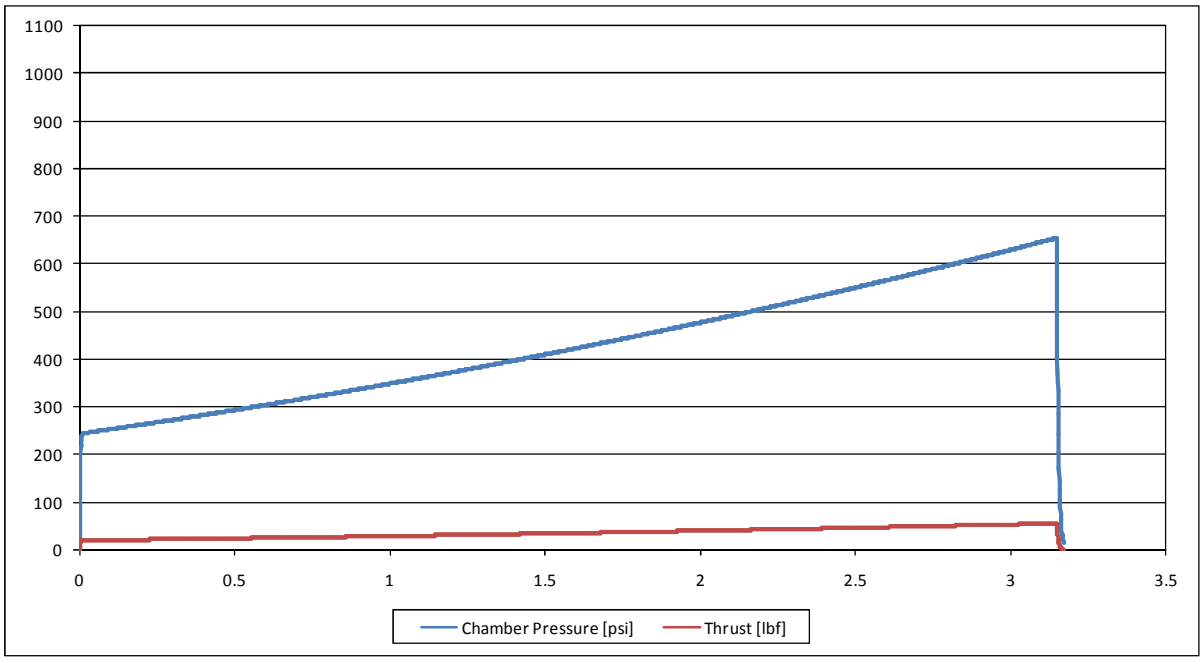

Figure 3.28: Motor firing #5 theoretical performance values as a function of time [s].

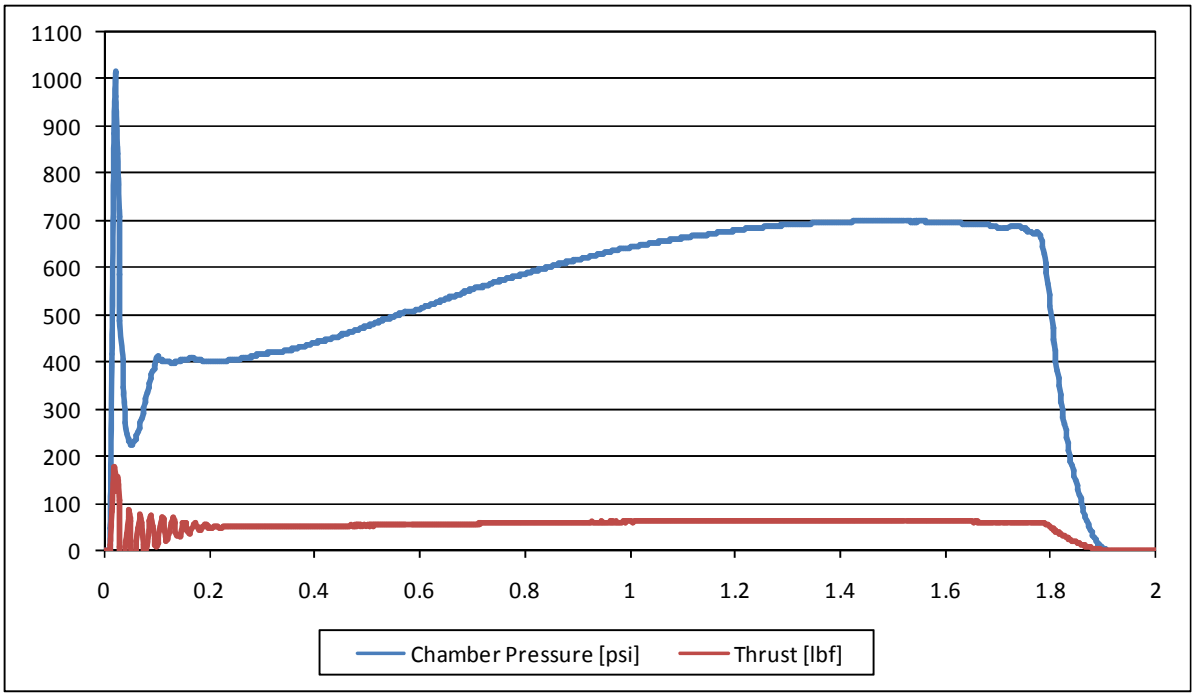

Figure 3.29: Motor firing #5 experimental performance values as a function of time [s].

3.9.7 Motor Firing #6

Aluminized grain
ID: .4375in.
OD: 2in.
L: 2.5in.
Nozzle Throat: Ø.3

Theoretical Prediction

Using the data from Appendix 1, the theoretical performance for this motor is shown in figure 3.30. Chamber pressure and thrust peaked at approximately $427\ psi$ and $36\ lbf$ respectively.

Experimental

Chamber pressure and thrust peaked at $371\ psi$ and $36\ lbf$ respectively as is seen in figure 3.31.

Comments

This firing is the first test to use a aluminized grain since firing #2. However, despite taking efforts to clean the interior burning surface, this grain didn't ignite until after the pressurization by the igniter was already lost. The interior surface was cleaned by first using a wire brush to remove the bulk of the Al_2O_3 buildup and then by very fine sandpaper to get the remainder. After the cleaning was completed, the interior surface of the grain was a much deeper black color than before. This is to be expected since the more oxide that has built up on the surface, the whiter the grain will appear. As can be seen from figure 3.31 however, this was a futile effort. This has two possible explanations. Firstly, the igniter was not burning hot enough to ignite the surface of the grain without a smoldering effect. Secondly, and more fundamentally, these propellant grains are approximately twenty five years old. While this didn't cause much of a concern with the non-aluminized grains, the aluminized grains seem to have degraded more seriously than their non-aluminized counterparts. This might be a hopeless endeavor due to age. Since creating a new igniter design was beyond the scope of this thesis, a method was attempted to make the existing igniter burn hotter without changing the system too much to draw acceptable conclusions between the two different grain compositions. In order to try to make the igniter burn hotter for the next run, two changes were made. First, when the igniter was assembled, powdered aluminum (~1μm diameter) was mixed in with the $BKNO_3$ in the igniter baggie. The second change was to use the powdered aluminum to coat the inner surface of the propellant grain in hopes of increasing the initial ignition temperature.

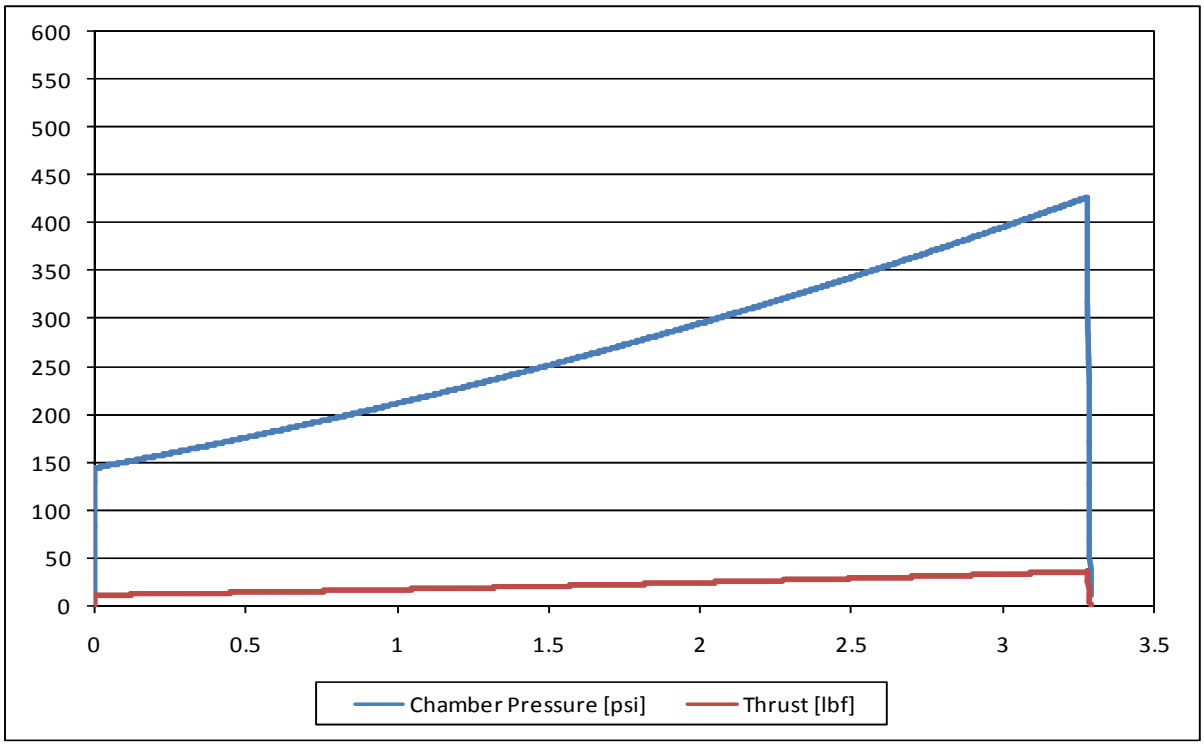

Figure 3.30: Motor firing #6 theoretical performance values as a function of time [s].

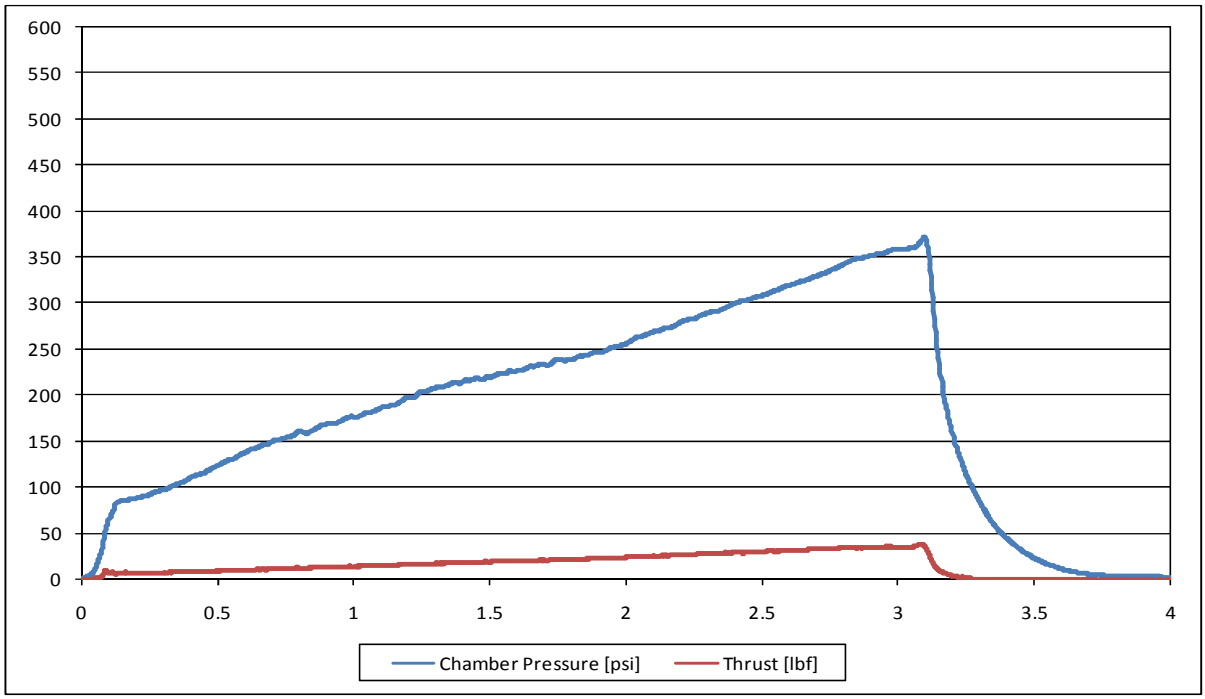

Figure 3.31: Motor firing #6 experimental performance values as a function of time [s].

3.9.8 Motor Firing #7

Aluminized grain
ID: .4375in.
OD: 2in.
L: 2.5in.
Nozzle Throat: Ø.3

Theoretical Prediction

Using the data from Appendix 1, the theoretical performance for this motor is shown in figure 3.32. Chamber pressure and thrust peaked at approximately $427\ psi$ and $36\ lbf$ respectively.

Experimental

Chamber pressure and thrust peaked at $370\ psi$ and $35\ lbf$ respectively as is seen in figure 3.33.

Comments

Figure 3.33 show the results of adding the powdered aluminum to the igniter and grain. The time lapse between the igniter firing and the grain firing decreased by 2.5 seconds but it's still not enough for the grain to ignite without losing its pressurization.

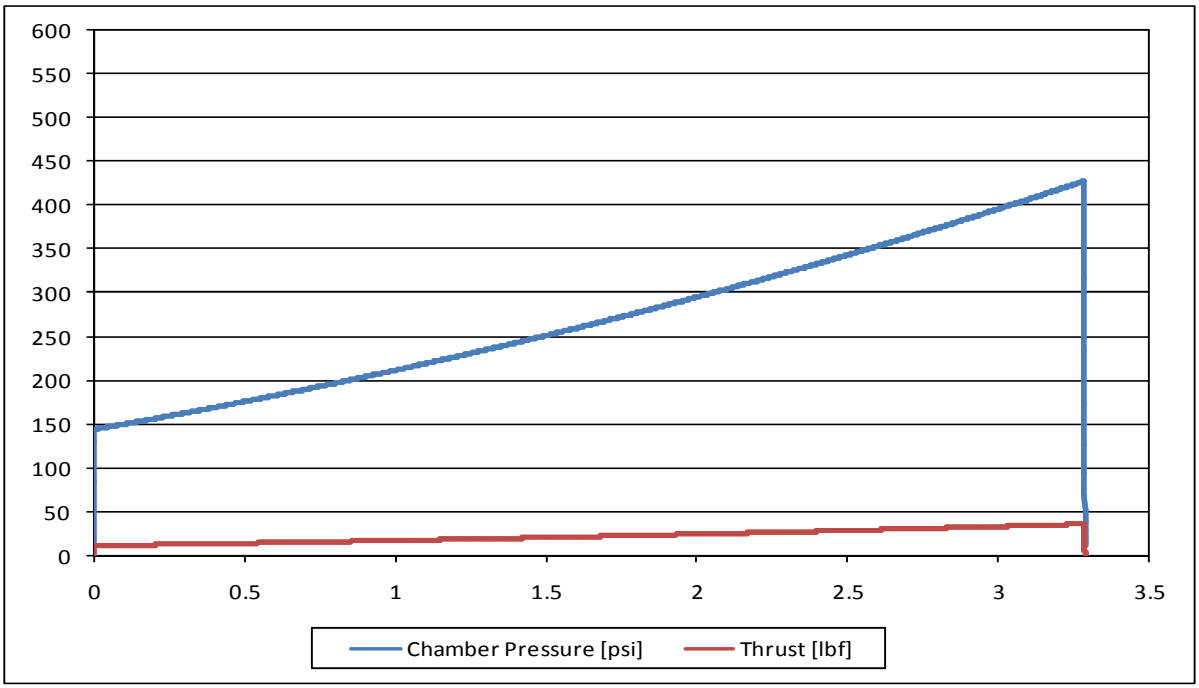

Figure 3.32: Motor firing #7 theoretical performance values as a function of time [s].

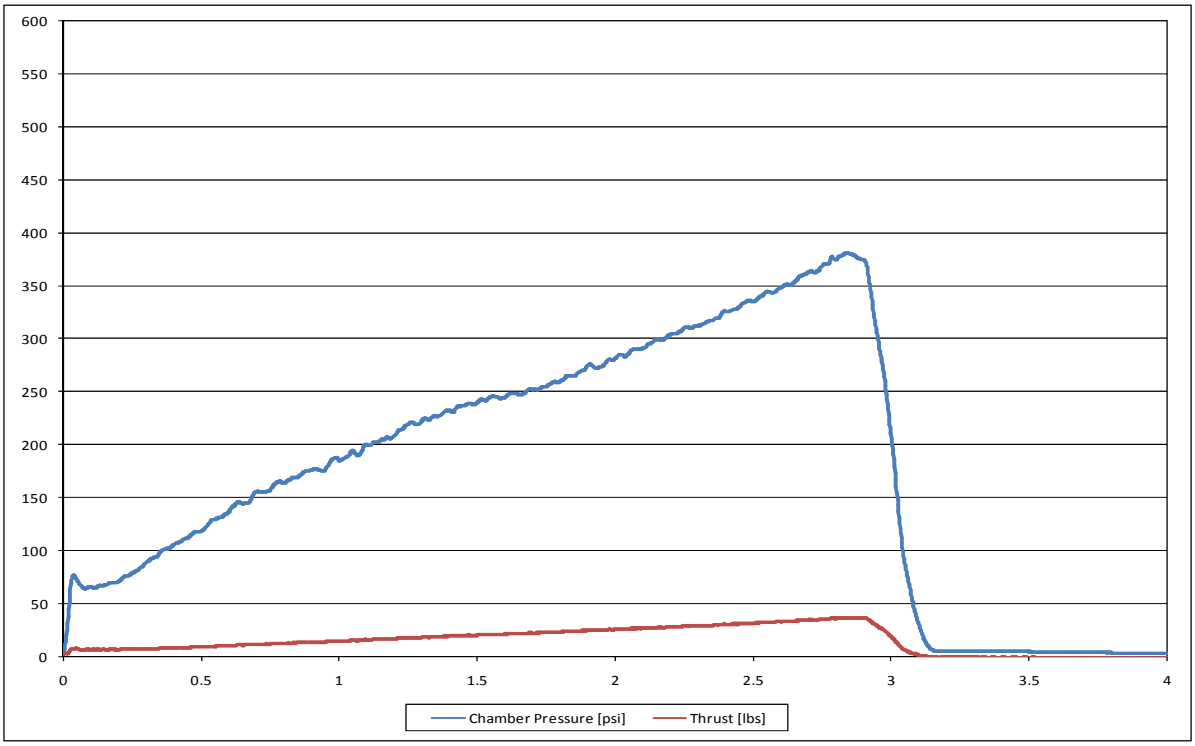

Figure 3.33: Motor firing #7 experimental performance values as a function of time [s].

3.9.9 Motor Firing #8

Aluminized grain
ID: .4375in.
OD: 2in.
L: 3in.
Nozzle Throat: Ø.3

Theoretical Prediction

Using the data from Appendix 1, the theoretical performance for this motor is shown in figure 3.34. Chamber pressure and thrust peaked at approximately $554\ psi$ and $47\ lbf$ respectively.

Experimental

Chamber pressure and thrust peaked at $456\ psi$ and $51\ lbf$ respectively as is seen in figure 3.35.

Comments

None

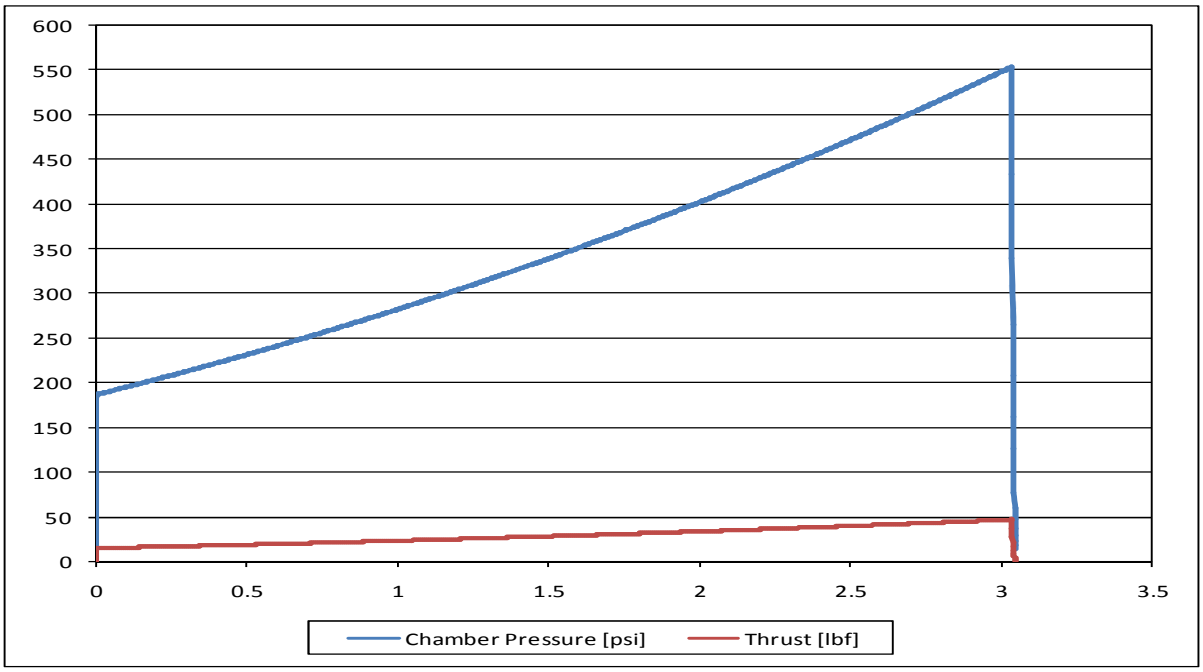

Figure 3.34: Motor firing #8 theoretical performance values as a function of time [s].

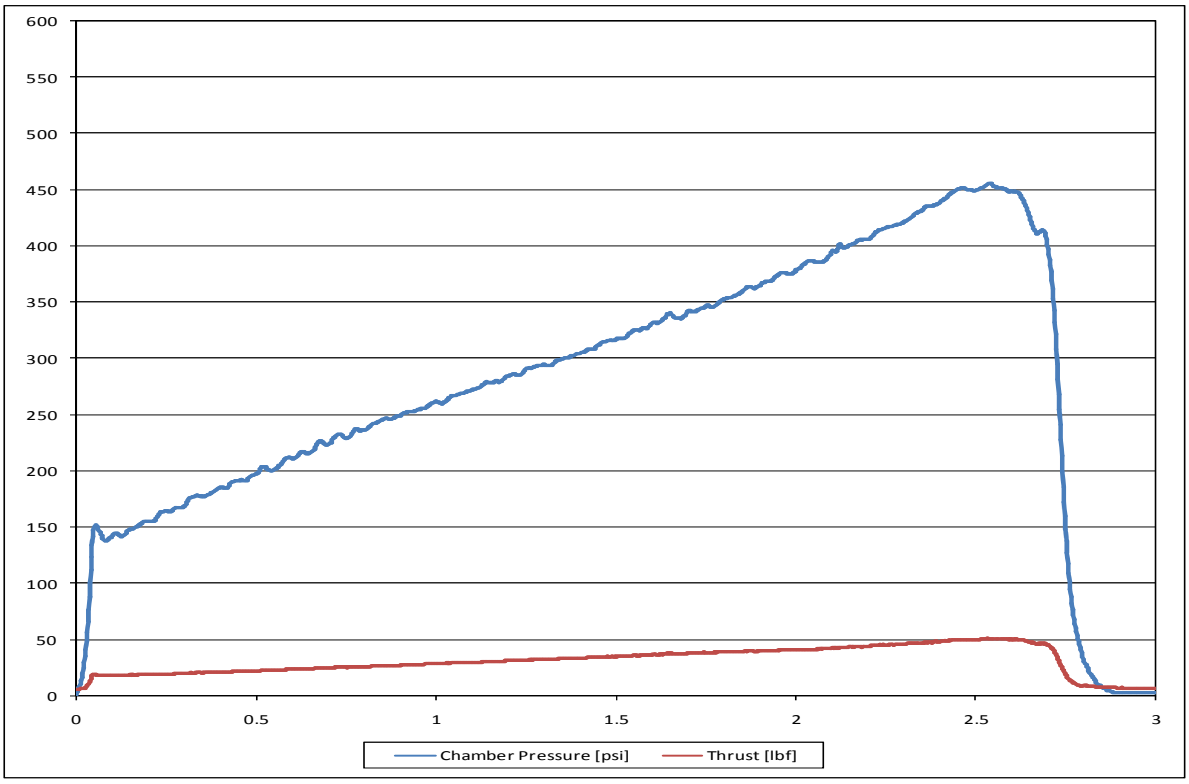

Figure 3.35: Motor firing #8 experimental performance values as a function of time [s].

3.10 Summary

For convenience, by combining the results that were obtained in section 3.9, table 3.3 is obtained.

Table 3.3

Experimental Data Collected

	Run 1	**Run 2**	**Run 3**	**Run 4**
Chamber Pressure [psi]	790	594	662	665
Thrust [lbf]	71	56	74	72
	Run 5	**Run 6**	**Run 7**	**Run 8**
Chamber Pressure [psi]	700	371	370	456
Thrust [lbf]	63	36	35	51

Chapter 4

Discussion and Conclusion

4.1 Preface

One of the objectives of this thesis has been to evaluate the performance increase due to aluminum as a energetic additive in solid rocket propellant. From the data gathered, the results can be summarized into four categories for comparisons. These are: non-aluminized theoretical vs. experimental comparisons, aluminized theoretical vs. experimental comparisons, aluminized theoretical vs. non-aluminized experimental comparisons, and I_{sp} comparisons. Following this, the other thesis objective is addressed, namely current thrust stand design evaluation. Finally, some words are said on future work. This includes both theoretical model and experimental improvements.

4.2 Experimental Comparisons

4.2.1 Non-Aluminized Theoretical vs. Experimental Comparisons

By combining the results that were shown in earlier in chapter three, one gets figures 4.1 and 4.2. This gives a better view for comparison of the different tests. The most obvious thing that is displayed is the variation between each run. In these four tests identical grains were used, the DAQ gave no errors or complications, and the grains performed satisfactorily. Even with these similarities, the chamber pressure still varied by as much as 19% and the thrust by 17%. This could be due to variation in initial propellant temperature, erosive burning effects, nozzle clogging, and other issues. These concepts were explained in more detail earlier in chapters two and three. The second thing is the overall comparison between the theoretical prediction and the experimental observations. Even with the assumptions that were listed in section 2.2, this simple model has delivered acceptable results. The shapes of the curves are different due to the pre-pressurization of the igniter baggie. This is the cause for the faster burns as seen in the experiments. By observing the maximum predicted performance, the theoretical chamber pressure is off by a maximum off 17% and a minimum of 1%. Likewise, the theoretical thrust is off by a maximum of 24% and a minimum of 11%. As expected, the thrust is more varied than the chamber pressure due to the steel plate burn out acting as a diffusing section as discussed in section 3.9.2. The full range of data is seen in table 4.1 with the percent difference to the theoretical prediction being shown.

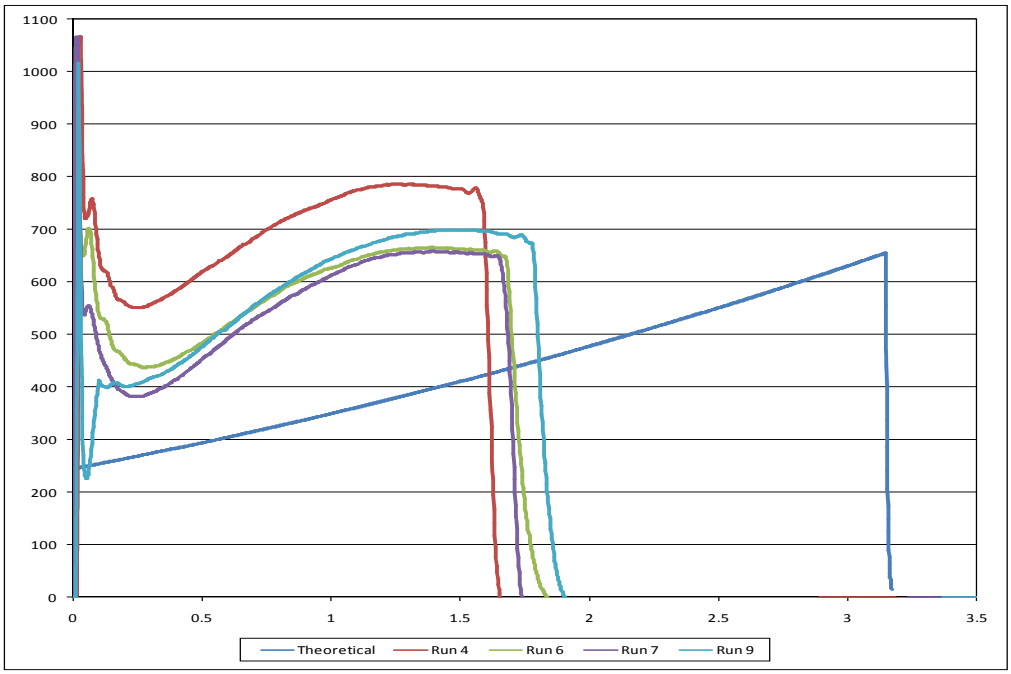

Figure 4.1: Non-aluminized theoretical and experimental comparisons of chamber pressure as a function of time [s].

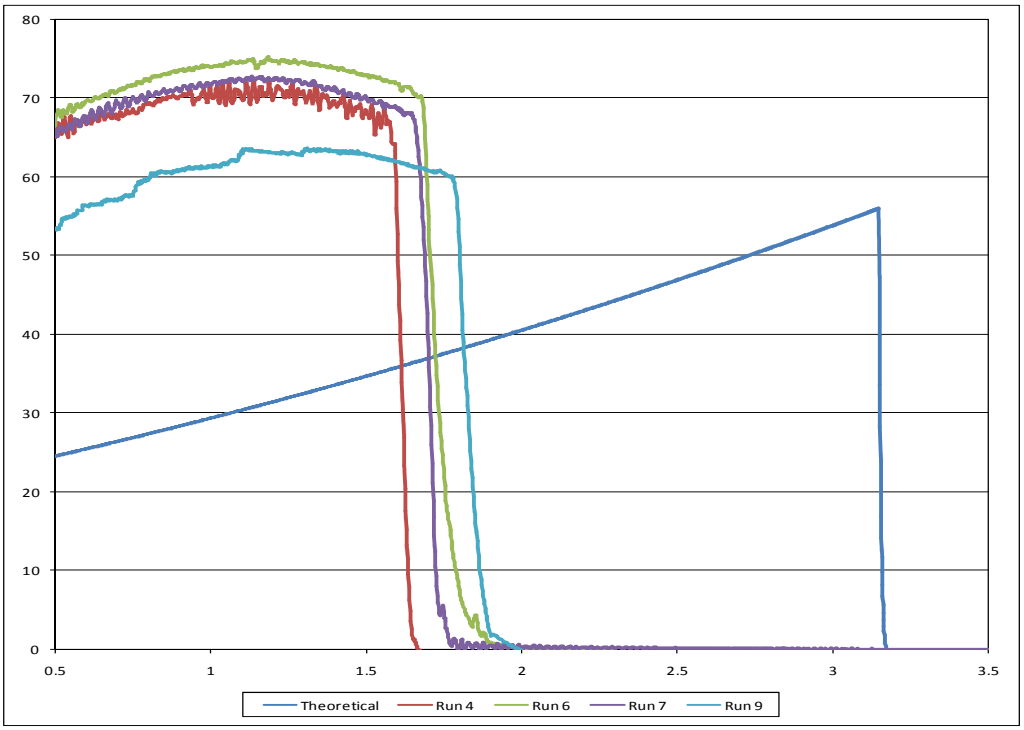

Figure 4.2: Non-aluminized theoretical and experimental comparisons of thrust as a function of time [s].

Table 4.1

Non-Aluminized Theoretical vs. Experimental Comparisons

	Theoretical	**Run 1**	**% Difference**	**Run 3**	**% Difference**
Chamber Pressure [psi]	655	790	17.1	662	1.1
Thrust [lbf]	56	71	21.1	74	24.3
	Theoretical	**Run 4**	**% Difference**	**Run 5**	**% Difference**
Chamber Pressure [psi]	655	665	1.5	700	6.4
Thrust [lbf]	56	72	22.2	63	11.1

4.2.2 Aluminized Theoretical vs. Experimental Comparisons

The aluminized tests cannot be displayed on a single figure like the non-aluminized. This is due to the variety of grain sizes. Firing information can be seen in table 4.2, again with the percent difference to the theoretical prediction being shown.

Table 4.2

Aluminized Theoretical vs. Experimental Comparisons

	Run 2 Theoretical	**Run 2**	**% Difference**	**Run 7 Theoretical**	**Run 7**	**% Difference**
Chamber Pressure [psi]	690	594	14	427	370	13
Thrust [lbf]	50	56	12	36	35	3
	Run 6 Theoretical	**Run 6**	**% Difference**	**Run 8 Theoretical**	**Run 8**	**% Difference**
Chamber Pressure [psi]	427	371	13	554	456	18
Thrust [lbf]	36	36	0	47	51	9

Even though the aluminized tests lost their pre-pressurization, they still exhibited a traditional burning profile once they ignited. The data compares with the theoretical model reasonably well, but not much can really be investigated without the initial pressurization. Because the data agrees however, it is a reasonable assumption that the theoretical model is underestimating the actual performance of these grains. Perhaps this lies in the assumptions in the model or perhaps this is due to the empirical coefficients used in the model. One can theorize issues on paper, but without further testing or existing data, nothing can be said with certainty.

4.2.3 Aluminized Theoretical vs. Non-Aluminized Experimental Comparisons

By using all of the information that has been obtained, one thing becomes very clear. The performance of the aluminized grains causes issues when trying to compare to their non-aluminized counterparts. This is due to the difficulties in igniting the aluminized grains and also due to the fact that there is not an aluminized grain that is the same size as a non-aluminized. Because of this, data shows some error in comparisons. At the same time, however, the theoretical model is sufficiently accurate for both grain types. This allows for a theoretical prediction of an aluminized grain that is the same size as a non-aluminized grain. The aluminized theoretical prediction for this case shows a maximum chamber pressure of $834\ psi$ and a maximum thrust of $72\ psi$. As shown in table 4.2, the chamber pressure in the aluminized grains was approximately 14% lower than the theoretical while the thrust was approximately 6% (median value) lower. By assuming that this latest prediction will follow the same trend, the theoretical performance can be adjusted to an expected chamber pressure of $717\ psi$ and $68\ lbf$ of thrust. This places the aluminized grain on the high end of the performance curve for chamber pressure without any initial pressurization when comparing with the non-aluminized tests. This is seen in figure 4.3 and figure 4.4, where the previous non-aluminized runs are shown for comparisons.

4.2.4 I_{sp} Comparisons

What has been shown so far is the measured performance data that has been obtained during these experiments. While chamber pressure and thrust data are informative to have, both are subjective when compared without identical test cases. Across these experiments, performance data was compared to firings that used different grain sizes, for example. In order to gain a better understand of the comparisons between these cases, the I_{sp} is used. This is seen in table 4.3. The non-aluminized grains varied from each other by no more than 4% and the aluminized grains offered a performance increase of 6% at a minimum. While firings two and seven produced expected chamber pressure and thrust data, the mass flow rate through the nozzle was much higher than other aluminized firings. This caused problems when doing I_{sp} comparisons, so the firings are omitted.

I_{sp} was obtained from equation 2.10 and by using the average thrust across a motor firing. This was defined as starting from 10% maximum chamber pressure and ending at pressure drop off at the end of the burn. The burn time was also defined in this way. Since the mass of the propellant is know, it was used to calculate the experimental mass flow rate. This enabled the experimental I_{sp} to be found.

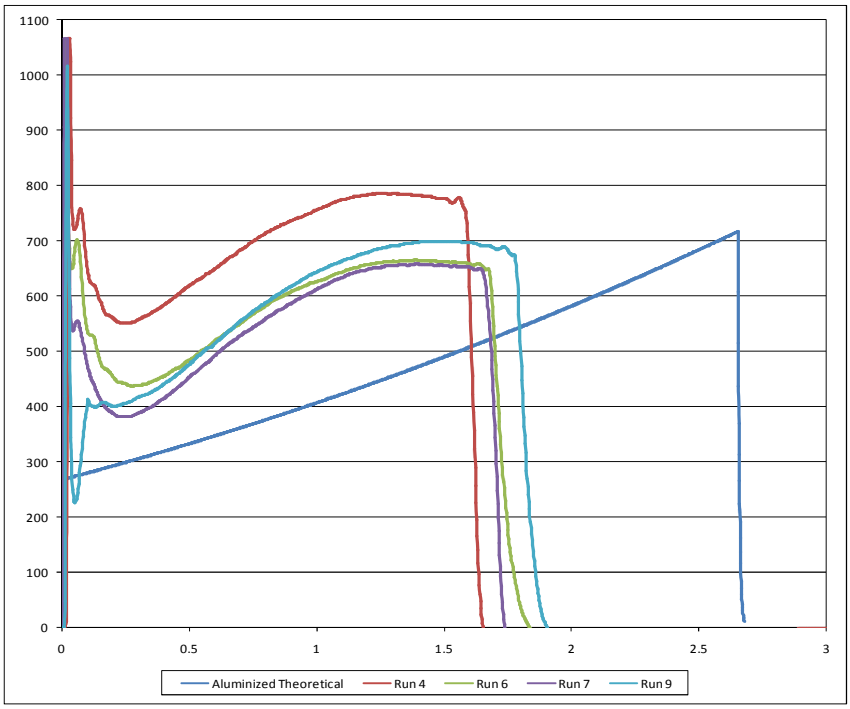

Figure 4.3: Aluminized prediction and non-aluminized experimental comparisons of chamber pressure as a function of time [s].

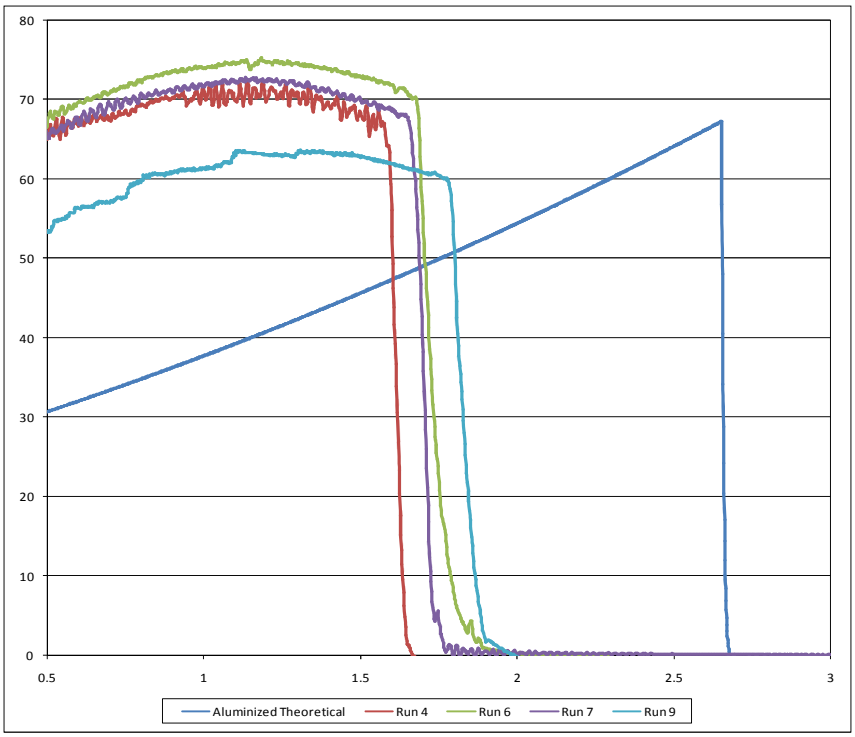

Figure 4.4: Aluminized prediction and non-aluminized experimental comparisons of thrust as a function of time [s].

Table 4.3

I_{sp} Comparisons

	Firing 1 Non-Aluminized	**Firing 3 Non-Aluminized**	**Firing 4 Non-Aluminized**
I_{sp} [s]	162	160	166
	Firing 5 Non-Aluminized	**Firing 6 2.5" Aluminized**	**Firing 8 3" Aluminized**
I_{sp} [s]	165	176	196

4.3 Thrust Stand Evaluation

Overall, this thrust stand design has worked quite well for this level of testing. When the top seals were blown during testing, the stand held up with virtually no damage. The worst that happened during testing was shearing a graphite nozzle. Once the igniter was changed to a $1{,}050\ psi$ "burst" and the back plate attached to reinforce the nozzle, there was concern about over pressurization; but after these tests, the stand has yet to show signs of failure. Another concern was if the graphite nozzle could withstand the heat from the gas flow, but it has remained in good condition after testing.

4.4 Future Work

There are three areas that can be improved in these experiments. First, the theoretical model can be more thorough. The current model did give good results, but it can be improved by relaxing some of the assumptions given in section 2.2. Improvements can also be made to the empirical coefficients governing St. Robert's Law. While the values that have been used in these experiments are accurate for the propellants in question, but they fail to represent one big issue, namely the age of the grains. Second, tests need to be conducted on newer grains. Newer grains will give more accurate data and should eliminate many of the ignition difficulties experienced in this set of tests. Third, improvements can be made in the experimental procedure itself. While this set of experiments was concerned with obtaining the chamber pressure and thrust of the available grains, a method to get real time information on the combustion chamber temperature would not only provide interesting data, it might also shed more light on the variation of performance between identical grains. Two changes could be made to the nozzle as well. The nozzle should be fabricated with a diverging section, whether one is interested in the change produced by the section or not. This will prevent having burnouts as encountered in firing #1 and allow a constant flow path for the hot gases, not have one that changes each run. Ideally you would want a different nozzle for each run, just for uniformity of test condition. While great effort was taken in this set

of experiments to remove any Al_2O_3 buildup after a firing, having different nozzles would have removed this problem all together.

List of References

Aerocon Systems. (n.d.). *Aerocon Systems Apparatus, Supplies, and Resources for Adventurers, Inventors, and Experimentors*. Retrieved May 16, 2011, from Aerocon Systems: http://aeroconsystems.com/cart/products/Horizontal_Vertical_Test_Stand_to_1500_LB_f_Thrust-159-0.html

Alliant Techsystems Inc. (2008, May 14). ATK Space Propulsion Products Catalog. Elkton, Maryland, United States of America.

Anderson, J. D. (2004). *Modern Compressible Flow with Historical Perspective.* New York: The McGraw-Hill Companies, Inc.

Arnold Air Force Base. (n.d.). *Arnold Air Force Base*. Retrieved May 16, 2011, from Arnold Air Force Base: http://www.arnold.af.mil/photos/mediagallery.asp?galleryID=3427

Bartley, C., Mills, M., & Huggett, C. (1960). *Solid Propellant Rockets.* Princeton: Princeton University Press.

Biblarz, O., & Sutton, G. P. (2001). *Rocket Propulsion Elements.* New York: Wiley-Interscience.

Brown, C. D. (1996). *Spacecraft Propulsion.* Washington, DC: American Institute of Aeronautics and Astronautics, Inc.

Hill, P. G., & Peterson, C. R. (1965). *Mechanics and Thermodynamics of Propulsion.* Reading: Addison-Wesley.

Humble, R. W., Henry, G. N., & Larson, W. J. (1995). *Space Propulsion Analysis and Design.* New York: The McGraw-Hill Companies, Inc.

Omega Engineering, Inc. (2011, July 22). *Sealed Beam Load Cells.* Retrieved July 22, 2011, from Omega.com Your One-Stop Source for Process Measurment and Control!: http://www.omega.com/Pressure/pdf/LCEC.pdf

Risha, G., Evans, B., Boyer, E., & Kuo, K. (2007). Metals, Energetic Additives, and Special Binders Used in Solid Fuels for Hybrid Rockets. In M. J. Chiaverini, & K. K. Kuo, *Fundamentals of Hybrid Rocket Combustion and Propulsion* (pp. 413-456). Reston: American Institute of Aeronautics and Astronautics, Inc.

Walker, M. (2005, October 9). *Solid Rockets & Aluminum*. Retrieved July 13, 2010, from http://www.aerospaceweb.org/question/propulsion/q0246.shtml

Appendices

Appendix 1

Table A.1

Existing Motor Performance

Characteristic	Star-48	Thiokol M55	Star-27
Motor Performance (70°F, sea level)			
Maximum thrust $[lbf]$	17,490	201,500	6,404 (vacuum)
Burn time average thrust $[lbf]$	15,430	194,600	6,010 (vacuum)
Action time average thrust $[lbf]$	15,370	176,600	5,177 (vacuum)
Maximum chamber pressure $[psi]$	618	850	569
Burn time average chamber pressure $[psi]$	579	780	552
Action time average chamber pressure $[psia]$	575	720	502
Burn time/action time $[s]$	84.1/85.2	52.6/61.3	34.35/36.93
Ignition delay time $[s]$	.099	.13	.076
Total impulse $[lbf \cdot s]$	1,303,705	10,830,000	213,894
Burn time impulse $[lbf \cdot s]$	---	10,240,000	---
Altitude specific impulse $[s]$	294.2	254	290.8 (vacuum)
Temperature limits $[°F]$	---	60 to 80	20 to 100
Propellant			
NH_4ClO_4 [%]	71	70	72
Aluminum [%]	18	16	16
Binder and additives [%]	11	14	12
Density $\left[\frac{lbm}{in^3}\right]$	.0651	.0636	.0641
Burning rate at 1000 psi $\left[\frac{in}{s}\right]$	.228	.349	.28
Burning rate exponent	.3	.21	.28
Temperature coefficient of pressure $[\%°F]$	.1	.102	.1
Adiabatic flame temperature $[°F]$	6,113	5,790	5,909
Characteristic velocity $\left[\frac{ft}{s}\right]$	5,010	5,180	5,180
Propellant Grain			
Type	Internal burning, radial slotted star	Six-point star	Eight-point star
Propellant volume $[in^3]$	68,050	709,400	11,480
Web $[in]$	20.47	17.36	8.17
Web fraction [%]	84	53.3	60
Sliver fraction [%]	0	5.9	2.6
Average burning area $[in^2]$	3,325	38,500	1,378
Volumetric loading [%]	93.1	88.7	---

Table A.1 (continued)

Igniter			
Type	---	Pyrogen	Pyrogen
Number of squibs	2	2	2
Minimum firing current $[A]$	5	4.9	5
Weights $[lbf]$			
Total	4,721	50,550	796.3
Total inert	290	4,719	60.6
Burnout	258	4,264	53.4
Propellant	4,431	45,831	735.7
Internal insulation	60	634	12.6
External insulation	---	309	0
Liner	2	150	.4
Igniter	---	26	2.9 (empty)
Nozzle	97	887	20.4
Thrust vector control device	---	Incl. with nozzle	0
Case	129	2,557	23.6
Miscellaneous	8	156	.7
Propellant mass fraction	.939	.912	.924
Dimensions			
Overall length $[in]$	---	294.87	48.725
Outside diameter $[in]$	---	65.69	27.3
Case			
Material	6A1-4V Titanium	Ladish D6AC steel	6 A1-4V titanium
Nominal thickness $[in]$	.069	.148	.035
Minimum ultimate strength $[psi]$	165,000	225,000	165,000
Minimum yield strength $[psi]$	155,000	195,000	155,000
Hydrostatic test pressure $[psi]$	732	940	725
Hydrostatic yield pressure $[psi]$	---	985	---
Minimum burst pressure $[psi]$	860	---	76.7
Typical burst pressure $[psi]$	---	---	---
Liner			
Material	TL-H-318	Polymeric	TL-H-304
Insulation			
Type	---	Hydrocarbon-asbestos	NA
Density $\left[\frac{lbm}{in^3}\right]$	---	.0394	---

Table A.1 (continued)

Nozzle			
Number and type	Fixed, contoured	4, movable	Fixed, contoured
Expansion area ratio	54.8/47.2	10:1	48.8/45.95
Throat area $[in^2]$	12.44	164.2	5.9
Expansion cone half angle $[deg]$	exit/eff, 14.3/16.3	11.4	Initial 18.9
Throat insert material	2D Carbon/Carbon	Forged tungsten	3D carbon-carbon
Shell body material	---	ANSI 4130 steel	NA
Exit cone material	Carbon Phenolic	NA	Carbon phenolic

NA: not applicable or not available (Biblarz & Sutton, 2001) & (Brown, 1996)

Appendix 2

Table A.2

Available Propellant Characteristics

Propellant Type	**Oxidizer Ratio** [%]	**Fuel Ratio** [%]	**Binder Ratio** [%]
AP\AL\HTPB*	.71	.18	.11
AP\HTPB	.89	0	.11

* Ammonium Perchlorate\Aluminum\Hydroxyl-terminated Polybutadiene

Compound	**Density** $\left[\frac{lbm}{in^3}\right]$
AP	.07046
AL	.09756
HTPB	.0336
Total*	.07128** , .06641***

* By weight
** Aluminized
*** Non-Aluminized

Number of Grains	**Inner Diameter** $[in]$	**Outer Diameter** $[in]$	**Grain Length** $[in]$	**Grain\Casing Volume** $[in^3]$	**Total Mass** $[lbm]$	**Oxidizer Mass** $[lbm]$	**Fuel Mass** $[lbm]$	**Binder Mass** $[lbm]$
1*	.875	1.875	3.5	7.559	.53883	.38257	.09699	.05927
1*	.875	1.875	3	6.48	.46191	.32796	.08314	.05081
2*	.875	1.875	2.5	5.4	.38493	.2733	.06929	.04234

* Aluminized

Number of Grains	**Inner Diameter** $[in]$	**Outer Diameter** $[in]$	**Grain Length** $[in]$	**Grain\Casing Volume** $[in^3]$	**Total Mass** $[lbm]$	**Oxidizer Mass** $[lbm]$	**Fuel Mass** $[lbm]$	**Binder Mass** $[lbm]$
4*	1	2	3.75	8.836	.58676	.52221	0	.06454

* Non-aluminized

Appendix 3

Table A.3

Variation of Calculated Performance Parameters for an Aluminized Ammonium Perchlorate Propellant as a Function of Chamber Pressure for Expansion to Sea Level

Chamber pressure $[psi]$	1,500	1,000	750	500	200
Chamber pressure $[psi]$ or pressure ratio $\frac{p_1}{p_2}$	102.07	68.046	51.034	34.023	13.609
Chamber temperature $[K]$	3,346.9	3,322.7	3,304.2	3,276.6	3,207.7
Nozzle exit temperature $[K]$	2,007.7	2,135.6	2,226.8	2,327	2,433.6
Chamber enthalpy $\left[\frac{cal}{g}\right]$	-572.17	-572.17	-572.17	-572.17	-572.17
Exit enthalpy $\left[\frac{cal}{g}\right]$	-1,382.19	-1,325.15	-1,282.42	-1,219.8	-1,071.2
Entropy $\left[\frac{cal}{g \cdot K}\right]$	2.1826	2.2101	2.2297	2.2574	2.32
Chamber molecular mass $\left[\frac{kg}{mol}\right]$	29.303	29.215	29.149	29.050	28.908
Exit molecular mass $\left[\frac{kg}{mol}\right]$	29.879	29.853	29.82	29.763	29.668
Exit mach number	3.2	3	2.86	2.89	2.32
Specific heat ratio - chamber	1.1369	1.1351	1.1337	1.1318	1.1272
Specific impulse, vacuum $[s]$	287.4	280.1	274.6	265.7	242.4
Specific impulse, sea level expansion $[s]$	265.5	256	248.6	237.3	208.4
Characteristic velocity, $\left[\frac{m}{s}\right]$	1,532	1,529	1,527	1,525	1,517
Nozzle area ratio, $\left[\frac{A_2}{A_t}\right]$ *	14.297	10.541	8.507	8.531	6.3
Thrust coefficient, $[C_F]$ *	1.7	1.641	1.596	1.597	1.529

* At optimum expansion (Biblarz & Sutton, 2001)

Appendix 4

Table A.4

MATLAB Validation Simulation Input for Existing Motors

Characteristic	Star-48	Thiokol M55	Star-27
Specific heat ratio	1.14	1.1337	1.1337
Combustion temperature $[K]$	3,651	3,472	3,538
Molar mass $\left[\frac{lbm}{lbmol}\right]$	29.3	28.28	28.28
Propellant density $\left[\frac{lbm}{in^3}\right]$	.0651	.0636	.0641
Temperature sensitivity coefficient $\left[\frac{in^{2n+1}}{lbf^{n} \cdot s}\right]$ *	.0287	.08	.035
Burning rate exponent	.3	.21	.28
Grain outer radius $[in]$	24.5	32.7	13.615
Nozzle throat radius $[in]$	1.99	7.23	1.37
Nozzle throat area $[in^2]$	12.441	164.22	5.896
Nozzle exit radius $[in]$	14.75	22.86	9.57
Nozzle exit area $[in^2]$	683.5	1,642.2	287.72
Effective grain inner radius$[in]$	5	15.485	5.95
Effective grain length $[in]$	50.909	294.87	24.362
Average combustion volume $[in^3]$	1,922	80,162	1,276
Average burning area $[in^2]$	3,325	38,500	1,378

* where n is the burning rate exponent

Appendix 5

Table A.5

MATLAB Firing Simulation Input Data

Characteristic	Firing 1	Firing 2	Firing 3	Firing 4
Specific heat ratio	1.1337	1.1337	1.1337	1.1337
Combustion temperature $[K]$	3,651	3,651	3,651	3,651
Molar mass $\left[\frac{lbm}{lbmol}\right]$	29.3	29.3	29.3	29.3
Propellant density $\left[\frac{lbm}{in^3}\right]$	.06641	.07128	.06641	.06641
Temperature sensitivity coefficient $\left[\frac{in^{2n+1}}{lbf^{n} \cdot s}\right]^{*}$	.026	.0287	.026	.026
Burning rate exponent	.3	.3	.3	.3
Grain outer radius $[in]$	1	.9375	1	1
Nozzle throat radius $[in]$	.15	.15	.15	.15
Nozzle throat area $[in^2]$	.0707	.0707	.0707	.0707
Nozzle exit radius $[in]$	.15	.15	.15	.15
Nozzle exit area $[in^2]$	.0707	.0707	.0707	.0707
Initial grain inner radius$[in]$	.5	.4375	.5	.5
Grain length $[in]$	3.75	3.5	3.75	3.75
	Firing 5	**Firing 6**	**Firing 7**	**Firing 8**
Specific heat ratio	1.1337	1.1337	1.1337	1.1337
Combustion temperature $[K]$	3,651	3,651	3,651	3,651
Molar mass $\left[\frac{lbm}{lbmol}\right]$	29.3	29.3	29.3	29.3
Propellant density $\left[\frac{lbm}{in^3}\right]$	.06641	.07128	.07128	.07128
Temperature sensitivity coefficient $\left[\frac{in^{2n+1}}{lbf^{n} \cdot s}\right]$ *	.026	.0287	.0287	.0287
Burning rate exponent	.3	.3	.3	.3
Grain outer radius $[in]$	1	.9375	.9375	.9375
Nozzle throat radius $[in]$	.15	.15	.15	.15
Nozzle throat area $[in^2]$	.0707	.0707	.0707	.0707
Nozzle exit radius $[in]$	.15	.15	.15	.15
Nozzle exit area $[in^2]$	.0707	.0707	.0707	.0707
Initial grain inner radius$[in]$	.5	.4375	.4375	.4375
Grain length $[in]$	3.75	2.5	2.5	3

* where n is the burning rate exponent

Appendix 6

Sample MATLAB Code Used for Theoretical Calculations

```
clear;
clc;
close all;
warning off all

%_____________________________________________________________________
%...Miscellaneous Constants
%_____________________________________________________________________

c1 = 32.2; %[(ft*lbm)/(lbf*s^2)]
go = 32.2; %[ft/s^2]

%_____________________________________________________________________
%...Constants
%_____________________________________________________________________

%...Ambient Pressure
Pa = 14.7; %[psi]
%_____________________________________
%...Specific Heat Ratio
ggamma = 1.1337;
%_____________________________________
%...Combustion Temperature
T_1 = 3651; %[K]
T_1 = T_1*1.8; %[R]
%_____________________________________
%...Molar Mass
M = 29.3; %[lbm/lbmol]
%...Ideal Gas Constant
R_bar = 1545; %[(ft*lbf)/(lbm*mole*R)]
%...Specific Gas Constant
R = R_bar/M*c1*12^2; %[in^2/(s^2*R)]
%_____________________________________
%...Propellant Density
rho_b = 0.0664054; %[lbm/in^3]
%_____________________________________
%...Temperature Coefficient
a = .026;
%...Burning Exponent
n = .3;
%_____________________________________
%...Grain Outer Radius
Ro = 2/2; %[in] w\o Al
%_____________________________________
%...Nozzle Throat Radius
Rt = .15; %[in]
%_____________________________________
%...Nozzle Throat Area
At = pi*(Rt)^2; %[in^2]
%_____________________________________
%...Nozzle Exit Radius
Re = Rt; %[in]
```

```
%_____________________________________
%...Nozzle Exit Area
Ae = pi*(Re)^2; %[in^2]

%_____________________________________________________________________________
%...Initial Conditions (t=0)
%_____________________________________________________________________________

%...Combustion Pressure
P_1(1) = Pa; %[psi]
%...Nozzle Exit Pressure
Pe(1) = Pa; %[psi]
%...Initial Time
t(1) = 0; %[s]
%_____________________________________
%...Grain Inner Radius
Ri(1) = 1/2; %[in] w\o Al
%_____________________________________
%...Grain Length
L(1) = 3.75; %[in]
%_____________________________________
%...Combustion Volume
V_1(1) = pi*(Ri(1)^2)*L(1); %[in^3]
%_____________________________________
%...Gas In Comustion Volume
mc(1) = 12*c1*P_1(1)*V_1(1)/(R*T_1); %[lbm]
%...Denisty of Gas in Combustion Volume
rho_c(1) = mc(1)/V_1(1); %[lbm/in^3]

if Ae==At
   Me = 1;
else
   %...Nozzle Exit Mach Number for a Diffuser Section
   eq1 = (Ae/At)^2;
   for Me = .001:.00001:10
      eq2 = (1/Me^2)*((2/(ggamma+1))*(1+((ggamma-1)/2)*Me^2))^((...
         ggamma+1)/(ggamma-1));
      if eq1 > eq2
         dummy_var1 = eq1/eq2;
      else
         dummy_var1 = eq2/eq1;
      end
      if dummy_var1 > 1.0001
         %...Blank
      else
         Mexit = Me;
         break;
      end
   end
   Me = Mexit;
end


%...Nozzle Exit Temperature
Te = 2*T_1/(2+Me^2*ggamma-Me^2); %[R]
```

```
%_____________________________________________________________________________
%...Burn Process
%_____________________________________________________________________________

i = 0;
dt = 0.001;
while Ri(i+1) <= Ro;
   i = i+1;
   %...Combustion Volume
   if i == 1
      %...No End Burning
      %_____________________________________
      V_1(i) = pi*Ri(i)^2*(L(1)); %[in^3]
      %_____________________________________
   else
      %...No End Burning
      %_____________________________________
      V_1(i) = pi*Ri(i)^2*(L(1)); %[in^3]
      %_____________________________________
   end

   %...Combustion Pressure
   P_1(i) = mc(i)*R*T_1/(V_1(i)*c1*12); %[psi]
   %...Regression Rate
   r(i) = a*P_1(i)^n; %[in/s]
   %_____________________________________
   %...Burning Area
   Ab(i) = 2*pi*Ri(i)*L(1); %[in^2]
   %_____________________________________
   %...Propellant Mass Flow Rate
   mdot1(i) = Ab(i)*rho_b*r(i); %[lbm/s]
   %...Nozzle Throat Mass Flow Rate
   mdot3(i) = 12*c1*At*P_1(i)*sqrt(ggamma/(R*T_1)*(2/(ggamma+1))^((...
      ggamma+1)/(ggamma-1))); %[lbm/s]
   %...Mass Flow Retained Through Combustion Volume
   mdot2(i) = mdot1(i) - mdot3(i); %[lbm/s]
   %...Mass in Combustion Volume
   mc(i) = 12*c1*P_1(i)*V_1(i)/(R*T_1); %[lbm]
   %...Denisty of Gas in Combustion Volume
   rho_c(i) = mc(i)/V_1(i); %[lbm/in^3]
   %...Nozzle Exit Pressure
   if i > 1
      Pe(i) = P_1(i)/((1+1/2*Me^2*ggamma-1/2*Me^2)^(ggamma/(...
         ggamma-1))); %[psi]
   else
   end
   %...Nozzle Exit Velocity
   Ve(i)= sqrt((2*ggamma*R*T_1)/(ggamma-1)*(1-(Pe(i)/P_1(i))^((...
      ggamma-1)/ggamma)))/12; %[ft/s]
   %...Thrust
   %_____________________________________
   F(i) = mdot3(i)*Ve(i)/c1 + (Pe(i) - P_1(1))*Ae; %[lbf] Sea Level
   %_____________________________________
   %...Specific Impulse
   Isp(i) = (F(i)*c1)/(mdot3(i)*go); %[s]
```

```
    if i >= 2
        %...Chamge in Chamber Pressure per Second
        dP_1(i)=(P_1(i)-P_1(i-1))/dt; %[psi/s]
    else
    end

    mc(i+1) = mc(i) + mdot2(i)*dt;
    Ri(i+1) = Ri(i) + r(i)*dt;
    L(i+1) = L(i) - r(i)*dt;
    t(i+1) = t(i) + dt;

end
t_plot1 = i;

while P_1(i) >= P_1(1)
    i = i+1;

    %...Burning Area
    Ab(i) = 0;
    %...Combustion Volume
    V_1(i) = V_1(i-1);
    %...Combustion Pressure
    P_1(i) = mc(i)*R*T_1/(V_1(i)*c1*12);
    %...Propellant Mass Flow Rate
    mdot1(i) = 0; %[lbm/s]
    %...Nozzle Throat Mass Flow Rate
    mdot3(i) = 12*c1*At*P_1(i)*sqrt(ggamma/(R*T_1)*(2/(ggamma+1))^((...
        ggamma+1)/(ggamma-1))); %[lbm/s]
    %...Mass Flow Rate Through Combustion Volume
    mdot2(i) = mdot1(i) - mdot3(i); %[lbm/s]
    %...Denisty of Gas in Combustion Volume
    rho_c(i) = mc(i)/V_1(i); %[lbm/in^3]
    %...Nozzle Exit Pressure
    Pe(i) = P_1(i)/((1+1/2*Me^2*ggamma-1/2*Me^2)^(ggamma/(...
        ggamma-1))); %[psi]
    %...Nozzle Exit Velocity
    Ve(i)= sqrt((2*ggamma*R*T_1)/(ggamma-1)*(1-(Pe(i)/P_1(i))^((...
        ggamma-1)/ggamma)))/12; %[ft/s]
    %_____________________________________
    %...Thrust
    F(i) = mdot3(i)*Ve(i)/c1 + (Pe(i) - P_1(1))*Ae; %[lbf] Sea Level
    %_____________________________________
    %...Specific Impulse
    Isp(i) = (F(i)*c1)/(mdot3(i)*go); %[s]

    mc(i+1) = mc(i) + mdot2(i)*dt;
    t(i+1) = t(i) + dt;

end

%_____________________________________________________________________________
%...Checks
%_____________________________________________________________________________

%...Regression Distance
[dummy_var1 k] = size(r);
```

```
j = 1;
while j <= k
   dr(j) = r(j)*dt;
   j = j + 1;
end
netdr = sum(dr);

clear dummy_var1 k
%...Total Impulse
[dummy_var1 k] = size(F);
j = 1;
while j <= k
   I(j) = F(j)*dt;
   j = j + 1;
end
Impulse = sum(I);

%_____________________________________________________________________________
%...Plots
%_____________________________________________________________________________

figure('Name','Combustion Pressure vs. Time');
plot(t(1:i),P_1);
title('Combustion Pressure vs. Time');
xlabel('T [s]');
ylabel('Combustion Presure [psi]');

figure('Name','Regression Rate vs. Time');
plot(t(1:t_plot1),r(1:t_plot1));
title('Regression Rate vs. Time');
xlabel('T [s]');
ylabel('Regression Rate [in/s]');

figure('Name','Burning Area vs. Time');
plot(t(1:t_plot1),Ab(1:t_plot1));
title('Burning Area vs. Time');
xlabel('T [s]');
ylabel('Burning Area [in^2]');

figure('Name','Combustion Volume vs. Time');
plot(t(1:t_plot1),V_1(1:t_plot1));
title('Combustion Volume vs. Time');
xlabel('T [s]');
ylabel('Combustion Volume [in^3]');

figure('Name','Mass in Chamber vs. Time');
plot(t(1:t_plot1),mc(1:t_plot1));
title('Mass in Chamber vs. Time');
xlabel('T [s]');
ylabel('Mass in Chamber [lbm]');

figure('Name','Nozzle Mass Flow Rate vs. Time');
plot(t(1:i),mdot3);
title('Nozzle Mass Flow Rate vs. Time');
xlabel('T [s]');
ylabel('Nozzle Mass Flow Rate [lbm\s]');
```

```
figure('Name','Combustion Chamber Volume vs. Time');
plot(t(1:i-1),V_1(1:i-1));
title('Combustion Chamber Volume vs. Time');
xlabel('T [s]');
ylabel('Combustion Chamber Volume [in^3]');

figure('Name','Gas Density in Chamber vs. Time');
plot(t(1:i-1),rho_c(1:i-1));
title('Gas Density in Chamber vs. Time');
xlabel('T [s]');
ylabel('Gas Density in Chamber [lbm/in^3]');

figure('Name','Nozzle Exit Pressure vs. Time');
plot(t(1:i),Pe);
title('Nozzle Exit Pressure vs. Time');
xlabel('T [s]');
ylabel('Nozzle Exit Presure [psi]');
ylim([0 1]);

figure('Name','Nozzle Exit Velocity vs. Time');
plot(t(1:i),Ve);
title('Nozzle Exit Velocity vs. Time');
xlabel('T [s]');
ylabel('Nozzle Exit Velocity [ft/s]');

figure('Name','Thrust vs. Time');
plot(t(1:i-1),F(1:i-1));
title('Thrust vs. Time');
xlabel('T [s]');
ylabel('Thrust [lbf]');

figure('Name','Specific Impulse vs. Time');
plot(t(1:i-1),Isp(1:i-1));
title('Specific Impulse vs. Time');
xlabel('T [s]');
ylabel('Specific Impulse [s]');
ylim([0 350]);
```

Appendix 7

Thrust Stand Drawings

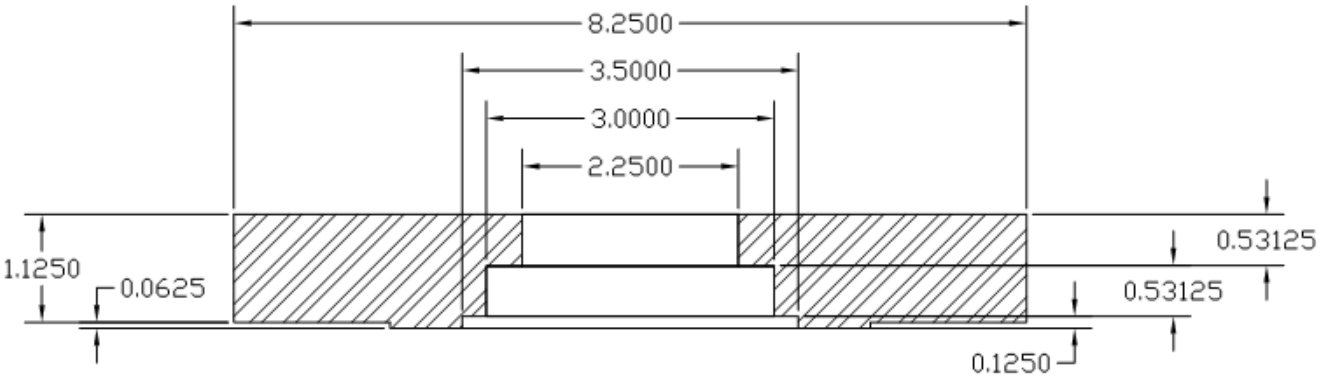

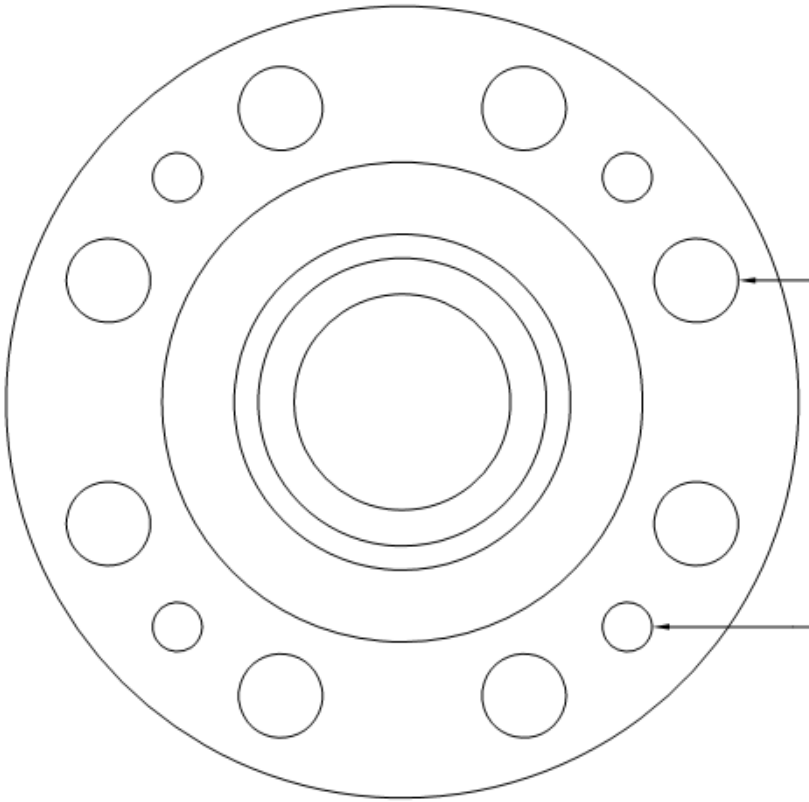

.875" Thru Holes
8 Places @ 45 Deg.
On 6.625" Dia. Center

.515" Thru Holes
4 Places @ 90 Deg.
On 6.625" Dia. Center

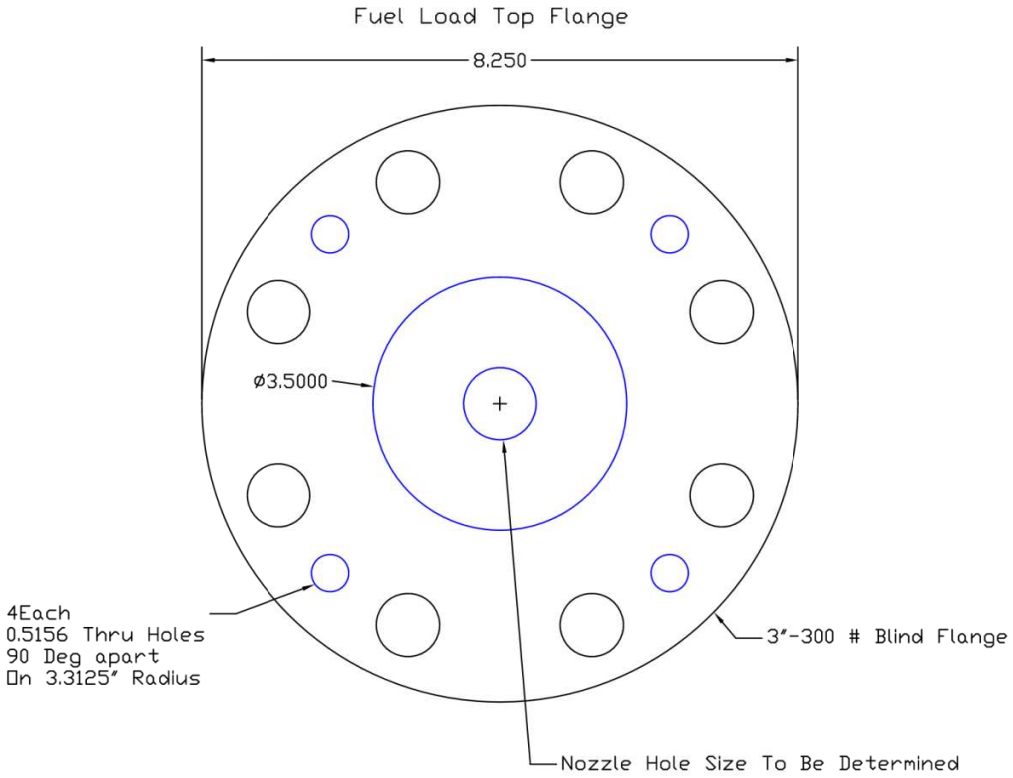
Fuel Load Top Flange
8.250
ø3.5000
4Each
0.5156 Thru Holes
90 Deg apart
On 3.3125" Radius
3"-300 # Blind Flange
Nozzle Hole Size To Be Determined

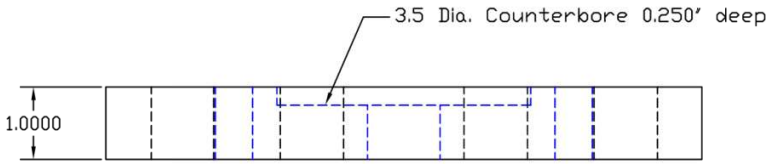
3.5 Dia. Counterbore 0.250" deep
1.0000

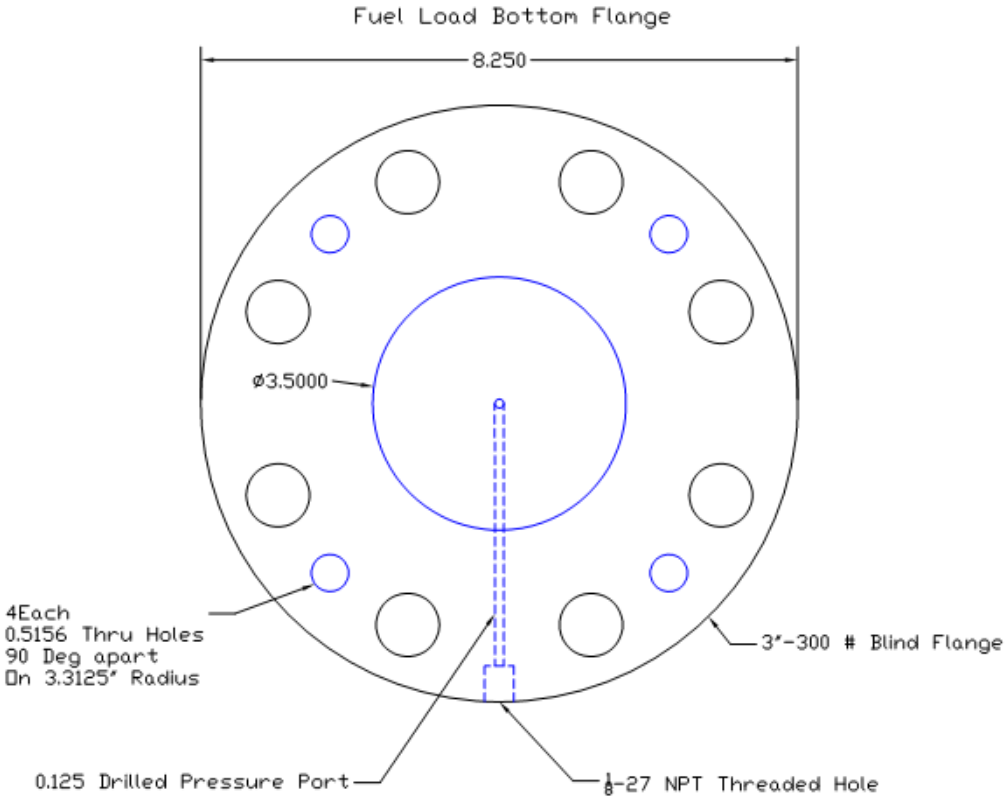
Fuel Load Bottom Flange
8.250
ø3.5000
4Each
0.5156 Thru Holes
90 Deg apart
On 3.3125" Radius
3"-300 # Blind Flange
0.125 Drilled Pressure Port
1/8-27 NPT Threaded Hole

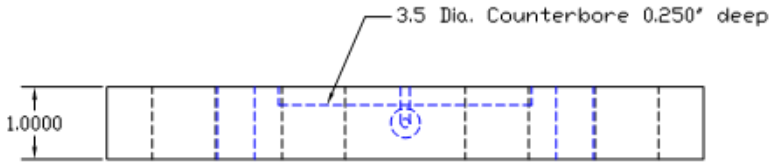
3.5 Dia. Counterbore 0.250" deep
1.0000

Fuel Load Cylinders
1 Each Material 1018 Steel

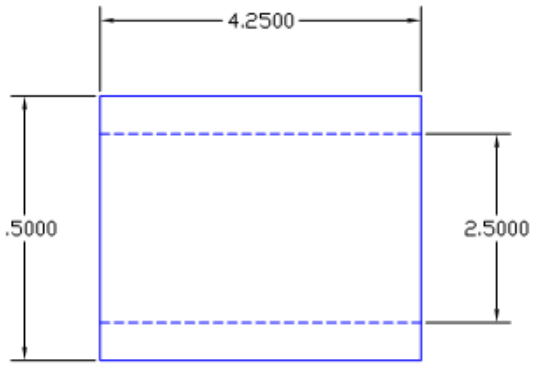

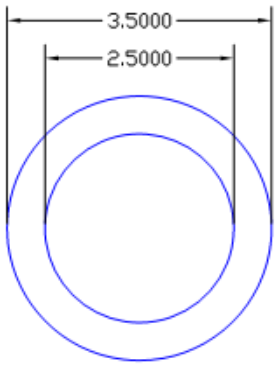

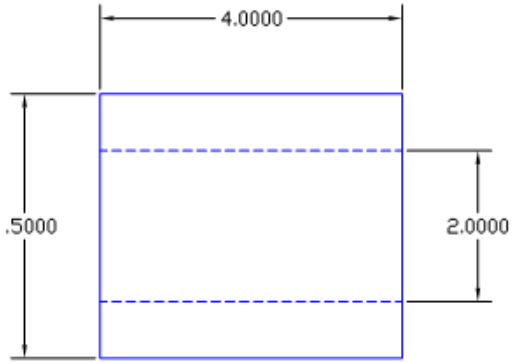

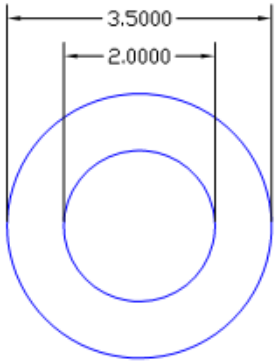

1 Each 0.52 Nozzle, Material Graphite

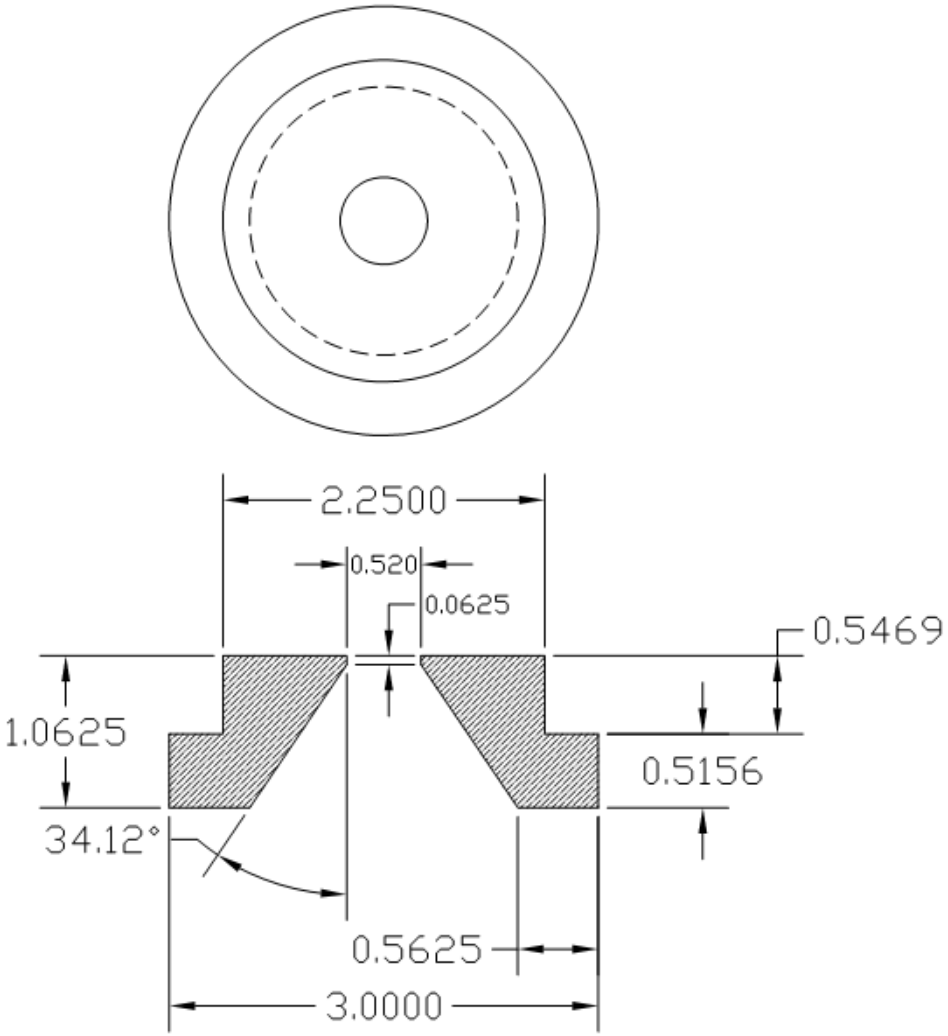

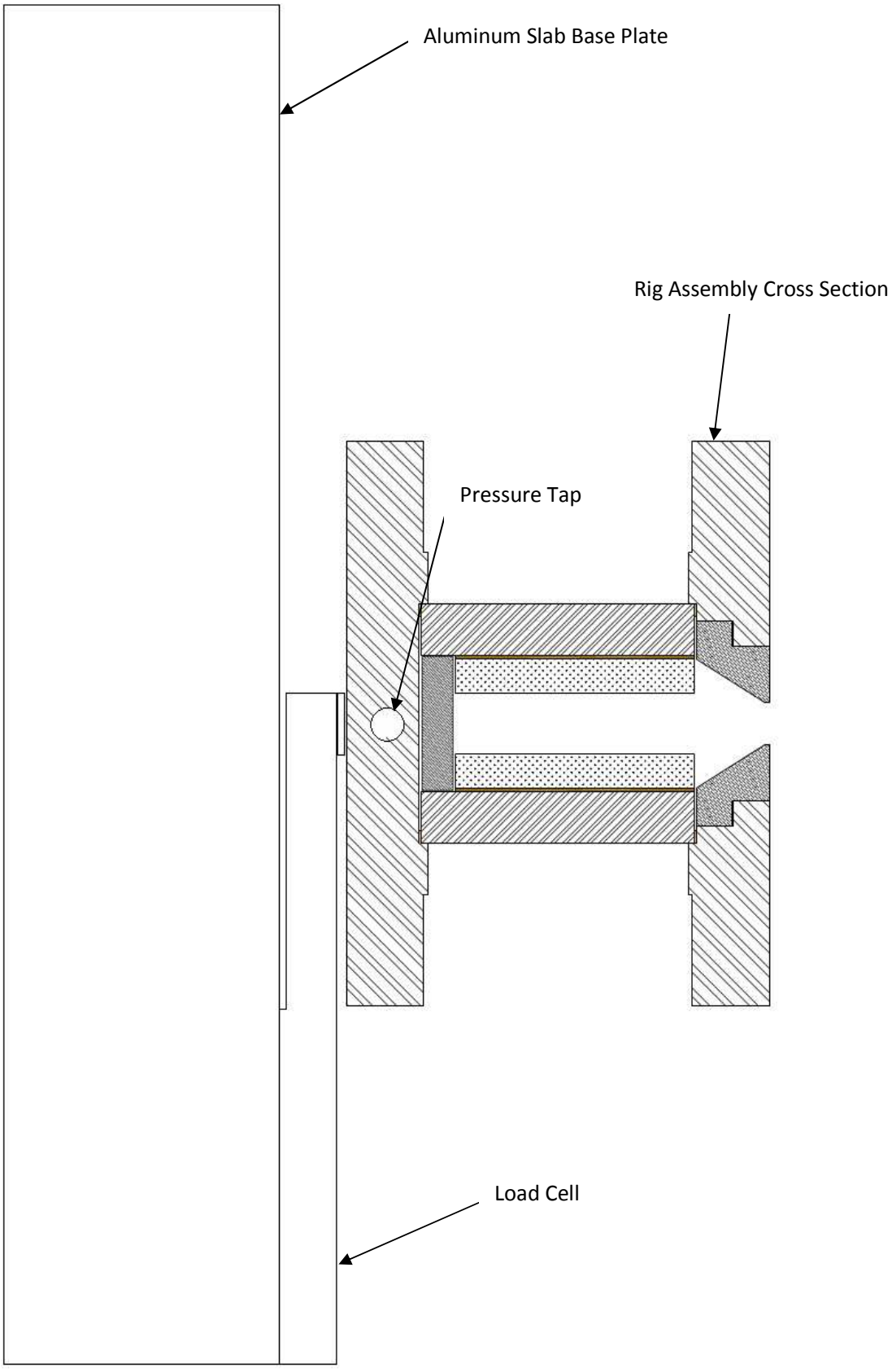
Aluminum Slab Base Plate
Rig Assembly Cross Section
Pressure Tap
Load Cell

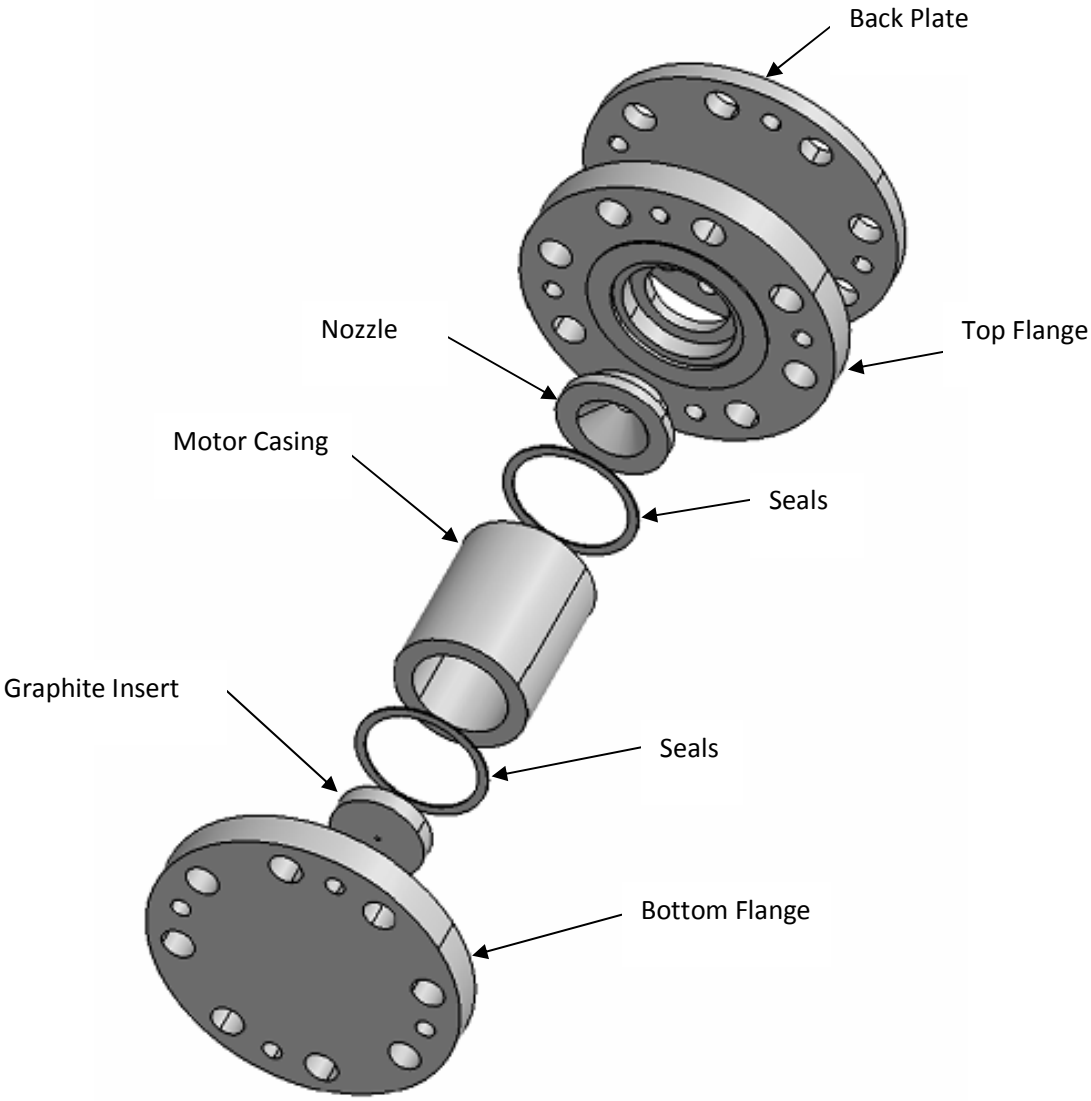
Back Plate
Nozzle
Top Flange
Motor Casing
Seals
Graphite Insert
Seals
Bottom Flange

Vita

Derek Damon Farrow was born in Rutledge, TN, to the parents of Damon and Annette Farrow. He attended Joppa Elementary and continued to Rutledge High School. After graduation, he moved to Daytona Beach, FL, where he attended Embry-Riddle Aeronautical University. While working in Information Technology he put himself through undergraduate and gained his Bachelors of Science in Aerospace Engineering with a concentration in Astrodynamics in 2008. Later that year he started attending the University of Tennessee Space Institute and later in 2009 he gained funding working for NASA on a grant for research into Energy Methods for Single-Stage-to-Orbit. Currently, Derek is finishing up his Masters of Science in Aerospace Engineering with a concentration in Space Engineering.